CAPITAL UNIVERSITY OF SCIENCE AND TECHNOLOGY, ISLAMABAD



Numerical Investigation of Thermal Boundary Value Problem of Mixed Convection Micropolar Flow

by

Marukh Ayub

A thesis submitted in partial fulfillment for the degree of Master of Philosophy

in the

Faculty of Computing
Department of Mathematics

2026

Copyright © 2026 by Marukh Ayub

All rights reserved. No part of this thesis may be reproduced, distributed, or transmitted in any form or by any means, including photocopying, recording, or other electronic or mechanical methods, by any information storage and retrieval system without the prior written permission of the author.



CERTIFICATE OF APPROVAL

Numerical Investigation of Thermal Boundary Value Problem of Mixed Convection Micropolar Flow

by

Marukh Ayub

(MMT243002)

THESIS EXAMINING COMMITTEE

S. No.	Examiner	Name	Organization
(a)	External Examiner	Dr. Saqib Zia	CUI, Islamabad
(b)	Internal Examiner	Dr. Abid Kamran	CUST, Islamabad

Dr. Muhammad Sabeel Khan
Thesis Supervisor
October, 2026

Dr. Muhammad Sagheer
Head
Dept. of Mathematics
October, 2026

Dr. Muhammad Abdul Qadir
Dean
Faculty of Computing
October, 2026

Author's Declaration

I, **Marukh Ayub** hereby state that my MPhil thesis titled "**Numerical Investigation of Thermal Boundary Value Problem of Mixed Convection Micropolar Flow**" is my own work and has not been submitted previously by me for taking any degree from Capital University of Science and Technology, Islamabad or anywhere else in the country/abroad.

At any time if my statement is found to be incorrect even after my graduation, the University has the right to withdraw my MPhil Degree.



(Marukh Ayub)

Registration No: MMT243002

Plagiarism Undertaking

I solemnly declare that research work presented in this thesis titled "**Numerical Investigation of Thermal Boundary Value Problem of Mixed Convection Micropolar Flow**" is solely my research work with no significant contribution from any other person. Small contribution/help wherever taken has been duly acknowledged and that complete thesis has been written by me.

I understand the zero tolerance policy of the HEC and Capital University of Science and Technology towards plagiarism. Therefore, I as an author of the above titled thesis declare that no portion of my thesis has been plagiarized and any material used as reference is properly referred/cited.

I undertake that if I am found guilty of any formal plagiarism in the above titled thesis even after award of MPhil Degree, the University reserves the right to withdraw/revoke my MPhil degree and that HEC and the University have the right to publish my name on the HEC/University website on which names of students are placed who submitted plagiarized work.



(Marukh Ayub)

Registration No: MMT243002

Acknowledgement

All the praise and appreciation are for almighty ALLAH who is the most beneficent and the most merciful created the universe and blessed the mankind with Intelligence and wisdom to discover His secrets. Countless respect and endurance for Prophet Muhammad (Peace Be Upon Him), the fortune of knowledge, who took the humanity out of ignorance and shows the right path. I would like to show my gratitude and immeasurable respect to my supervisor Dr. Muhammad Sabeel Khan, Associate Professor, Capital University of Science and Technology, Islamabad for his continuous guidance, willingness to assist and encouragement throughout this research. I deem it as my privilege to work under his incredible supervision.

I am extremely grateful to all of my teachers for their encouragement and emphasis on striving for excellence when teaching mathematics. I would also like to thanks CUST, For giving me such a conductive setting for this research. At this juncture, I pay deep regards and thanks to my beloved parents, whose selfless care, love, devotion and prayers have made me able to achieve this goal. Lastly, I would like to thanks my husband for his countless support and my all family members.



(Marukh Ayub)

Registration No: MMT243002

Abstract

This thesis presents a numerical investigation of transient mixed convection micropolar fluid flow and heat transfer in a two-dimensional enclosure using the Galerkin Finite Element Method (FEM). The mathematical model consists of the continuity equation, momentum equations, microrotation equation, and energy equation formulated under the assumptions of incompressible and laminar flow. The governing equations are first transformed into their corresponding weak (variational) forms using the Galerkin weighted residual approach and subsequently discretized using finite element basis functions. Temporal discretization is performed using the implicit backward Euler scheme, resulting in a stable and efficient numerical formulation. The resulting nonlinear algebraic system is implemented and solved using the finite element in FreeFEM++. The accuracy and reliability of the developed numerical model are established through validation with the benchmark results for the classical lid-driven cavity flow problem. An excellent agreement is obtained between the present numerical solutions and the benchmark data, confirming the correctness of the finite element implementation. A detailed parametric study is conducted to examine the influence of the Reynolds number (Re), Grashof number (Gr), Prandtl number (Pr), micropolar coupling parameter (K), and Eringen parameter (Er) on the velocity, microrotation, and temperature fields. The numerical results are presented through contour plots and quantitative comparisons at selected monitoring locations. The study reveals that increasing the Reynolds number enhances the dominance of inertial forces, resulting in stronger flow circulation and thinner momentum boundary layers. An increase in the Prandtl number reduces thermal diffusivity, thereby producing thinner thermal boundary layers and steeper temperature gradients near the heated wall. The micropolar coupling parameter is found to have a pronounced influence on both the microrotation and velocity fields by strengthening the interaction between the translational and rotational motions of the fluid microelements. Conversely, increasing the Eringen parameter suppresses the rotational response of the microelements by weakening the coupling between the microrotation and fluid vorticity, leading to a reduction in the magnitude of the microrotation field while exerting only a minor influence on the translational

velocity. Overall, the present investigation demonstrates the capability of the Galerkin finite element formulation implemented in FreeFEM++ to accurately simulate transient mixed convection micropolar flows with heat transfer. The results provide valuable insights into the combined effects of fluid inertia, buoyancy, thermal diffusion, and micropolar characteristics, thereby contributing to a better understanding of heat and momentum transport in micropolar fluids encountered in engineering and industrial applications.

Contents

Author's Declaration iii

Plagiarism Undertaking iv

Acknowledgement v

Abstract vi

List of Figures x

List of Tables xi

Abbreviations xii

Symbols xiii

1 Introduction and Literature Review 1
- 1.1 Introduction . . . 1
- 1.2 Literature Review . . . 4
- 1.3 Thesis Contribution . . . 8
- 1.4 Thesis Objectives . . . 9
- 1.5 Thesis Layout . . . 9

2 Basics of Finite Element Method 11
- 2.1 The Basic concept of Finite Element Method . . . 11
  - 2.1.1 Discretization of the Domain . . . 12
  - 2.1.2 Approximation of Field Variables . . . 12
  - 2.1.3 The Method of Weighted Residual . . . 13
  - 2.1.4 Galerkin Finite Element Formation . . . 15
  - 2.1.5 Weak Formulation . . . 16
  - 2.1.6 Element Matrices . . . 16
  - 2.1.7 Assembly Process . . . 17
  - 2.1.8 Boundary Conditions . . . 17
  - 2.1.9 Solution of Algebraic System . . . 19
  - 2.1.10 Advantages of FEM . . . 19

2.1.11 Worked Example: Nonlinear Convection Diffusion Equation 19
2.1.11.1 Weak Formulation . . . 20
2.1.11.2 Finite Element Discretization . . . 20
2.1.11.3 Element Matrices and Force Vector . . . 21
2.1.11.4 Element Stiffness Matrix . . . 22
2.1.11.5 Nonlinear Convection Matrix . . . 22
2.1.11.6 Element Force Vector . . . 23
2.1.11.7 Assembly of the Global System . . . 23
2.1.11.8 Application of Boundary Conditions . . . 24
2.1.11.9 Summary of the Worked Example . . . 24
2.2 Introduction to FreeFEM++ . . . 25
2.2.1 Formation of FreeFEM++ . . . 25
2.2.2 Significance of FreeFEM++ . . . 25
2.2.3 Advantages of Using FreeFEM++ . . . 26
2.2.3.1 FreeFEM++ Implementation Algorithm . . . 26

3 Mathematical Equations 28
3.1 Physical Description of the Problem: . . . 28
3.2 Mathematical Model . . . 29
3.2.1 Governing Equations in Dimensional Form . . . 29
3.2.2 Conversion of Dimensional Form into Dimension-less Form . 31
3.3 Numerical Procedure of Galerkin Based Finite Element Formation . 39
3.3.1 Variational Formation . . . 39
3.3.2 Finite Element Approximation . . . 45
3.3.3 Assembly of the Global System of Equations . . . 50
3.3.4 Temporal Discretization using the Backward Eular Method . 51
3.4 Numerical Solution Algorithm . . . 54
3.5 Implementation in FreeFEM++ . . . 55
3.5.1 Numerical Procedure for implementation in FreeFEM++ . . 55

4 Results and Discussion 57
4.1 Validation of Numerical Results . . . 57
4.2 Calculations of Results . . . 60

5 Conclusion and Future Directions 82
5.1 Conclusion . . . 82
5.2 Future Work . . . 84

Bibliography 86

List of Figures

3.1 Schematic representation of the computational domain and boundary configuration. 29

4.1 Temperature streamlines for varying values of the Prandtl number. Other parameters used are $Re = 10$, $Gr = 0.5$, $Er = 0.3$. 63
4.2 Temperature streamlines for varying values of the Eringen number. Other parameters used are $Re = 10$, $Gr = 0.5$, $Pr = 0.3$, $K = 5.5$. 66
4.3 U-velocity profiles for varying values of the Reynolds number. Other parameters used are $Gr = 0.5$, $Pr = 0.3$, $K = 5.5$, $Er = 0.3$. 69
4.4 Microrotation velocity profiles for varying values of the Micropolar parameter. Other parameters used are $Re = 1.0$, $Gr = 0.5$, $Pr = 0.3$, $K = 0.005$, $Er = 0.3$. 71
4.5 Microrotation velocity profiles for varying values of the Eringen number. Other parameters used are $Re = 1.0$, $Gr = 0.5$, $Pr = 0.3$, $K = 0.005$, $Er = 3.3$. 74

List of Tables

4.1 Validation of U-velocity with absolute error compared to Ghia et al. [35]. 59
4.2 Validation of V-velocity with absolute error compared to Ghia et al. [35]. 59
4.3 Variation of W at different locations for different values of Eringen number Er. Other parameters are $Re = 1.0$, $Gr = 0.5$, $Pr = 0.3$, $K = 0.005$. 73
4.4 Variation of W at different locations for different values of micropolar coupling parameter K. 76
4.5 Variation of velocity U at different locations for different values of micropolar parameter K. 78
4.6 Variation of velocity U at different locations for different values of Eringen number Er. 79

Abbreviations

BC	Boundary Condition
BE	Backward Eular
CFD	Computational Fluid Dynamics
Er	Eringen number
FEM	Finite Element Method
FreeFEM++	Finite Element Method software
GFEM	Galerkin Finite Element Method
Gr	Grashof number
IC	Initial Condition
K	Micropolar coupling parameter
MHD	Magnetohydrodynamics
MP	Micropolar
MR	Microrotation
Nu	Nusselt Number
P_1	Linear Polynomial Finite Element
P_2	Quadratic Polynomial Finite Element
PDEs	Partial Differential Equations
Pr	Prandtl number
Re	Reynolds number

Symbols

F	load vector
G	pressure gradiant matrix
K	micropolar coupling parameter
K_m	stiffness matrix
M	mass matrix
N	convection matrix
N_i	finite element shape function
P	dimensionless pressure
T	dimensionless time
U	x-component of velocity
V	y-component of velocity
W	dimensionless microrotation
x, y	cartesian coordinates
Γ	boundary of computational domain
γ	spin gradiant viscosity
η	temperature test function
θ	dimensionless temperature
κ	vortex viscosity
μ	dynamic viscosity
ρ	fluid density
Φ	continuity test function
Φ_1, Φ_2	velocity test function
Ψ	microrotational test function
Ω	computational domain

Chapter 1

Introduction and Literature Review

1.1 Introduction

The research dealing with transfer of heat and flow of fluids within closed cavities with heated obstacles has received a lot of interest and attention in engineering and industry due to its many applications. These include electronic cooling systems, heat exchangers, lubrication technologies, ventilation systems, chemical processing equipment, solar collectors, nuclear reactors and biomedical devices [1], [2], [3]. The problem of heat transfer through a cavity with fins, obstacles, cylinders and baffles has been receiving a significant amount of attention in recent years because of its significance in thermal management and energy systems as demonstrated in a recent systematic review by Al-Amiri et al. [4]. Buoyancy effects on fluid motion in the enclosure interact with the external forcing and lead to mixed convection phenomena in many practical situations.

Mixed convection occurs when both forced convection and natural convection play a significant role on the momentum and heat transfer in the fluid domain [5]. If heated obstacles are placed in such type of cavity, the thermal and flow properties of the cavity are greatly altered. Recirculation regions, thermal plumes

and secondary vortices formed by heated obstacles have a significant impact on the performance of heat transfer. The distribution of streamlines, temperature contours and thermal boundary layers within the enclosure are affected by the geometry, dimensions and position of the obstacles [6] .

Thus, the study of mixed convection flow in cavity containing heated obstacles is an important problem for which study in computational fluid dynamics and heat transfer has become important. The conventional models of Newtonian fluids are not adequate to describe the behavior of micro-structural fluids like polymeric suspensions, blood, colloidal fluids, liquid crystals, lubricants with additives etc. To overcome these limitations, A.C. Eringen introduced the theory of micropolar fluids, a class of non Newtonian fluids that accounts for the microscopic rotational motion of fluids particle and the associated couple stress effects [7].

In micropolar fluid theory, particles are assumed to undergo independent rotation in addition to translational motion. This rotational motion is represented by an additional physical variable known as microrotation, which describes the angular velocities of micro elements within the fluid and it plays a significant role in the internal spinning effects of microstructure fluid and does have some extra equations, to account for angular momentum and microrotation effects and is more suitable for the analysis of complex fluids found in industry and biology, in comparison to classical fluid mechanics [8]. The microrotation effect in square cavities with heated obstacles become more significant due to the presence of walls and obstacle modifies rotational interaction between layers of fluid. It also interacts with buoyancy forces and effects of forced convection. The flow inside the rectangular geometry with heated obstacles is a highly non linear and coupled thermo-fluid problem, due to the presence of micropolar fluid.

The governing equations are difficult to obtain analytical solutions for practical geometries and boundary conditions and include the continuity, momentum, angular momentum and energy problems. Hence, numerical methods are frequently used to study such problems. The Finite Element Method (FEM) is one of the most reliable and flexible numerical methods for solving the equations of fluid flow and

heat transfer, particularly in problems involving complex geometries and boundry conditions ([9], [10]). FEM transform the partial differential equations (PDEs) into weak forms and approximates their solutions over the discretized finite elements [11]. This method provides accurate approximations of the velocity, pressure, temperature and microrotational fields while maintaining numerically stability and convergence under appropriate discritization [12]. The system of governing equations are solved numerically by the method of Finite Elements using software FreeFEM++.It is an open source finite element software with the emphasis on numerical solution of partial differential equations. It offers flexibility in terms of the generation of the mesh, the implementation of the weak formation and the numerical approximation of coupled nonlinear equations [13]. FreeFEM++ is widely used in simulations of fluids and heat transfer, because of its high-performance finite element framework and its ability to stimulate complex computational domains. Various researchers have studied the mixed convection and micro-polar flow in cavities with varying thermal and physical conditions. Previous studies showed that Reynolds number Re, Grashof number Gr, Prandtl number Pr, vortex viscosity parameter, obstacle arrangement and thermal boundary conditions are important factors which influence the circulation of the fluid, microrotation behavior and heat transfer rates ([14], [15], [16], [17]).

But there is very little work available for thermal boundary value problems with heated obstacles in the presence of mixed convection micropolar flow in square geometries using detailed finite element formulation and implementation in FreeFEM++.So, this present thesis is mainly inclined on the numerical study of thermal boundary value problems of the mixed convection micropolar flow in a square geometry with heated obstacles. The weak formulations of the governing equations are formulated and discretized by FEM. Important physical parameters which affect the streamline pattern, isotherms, microrotaion distribution and heat transfer characteristics are analyzed in detail. The main goal of the study is to gain a comprehensive knowledge of the micropolar convection phenomena and to illustrate the usefulness of the FEM and FreeFEM++ in the solution of complex thermo-fluid problems.

1.2 Literature Review

The theory of micropolar fluids started with the work of A.C. Eringen [7] which introduced the mathematical model of a fluid that exhibits micro-structure effects. His theory included the effect of microrotation and couple stresses which are not included in classical Navier-Stokes equations.This theory paved the way to subsequent studies on micropolar convection and heat transfer. Jena and Bhattacharyya [18] investigated thermal convection in micropolar fluid confined between rectangular enclosures and proved that the phenomenon of convection and thermal stability is highly influenced by micropolar parameters. Their research showed that the onset of convection is greatly affected by the microrotation effects, when compared with Newtonian fluids. Hsu and Chen [19] studied the micropolar flow with natural convection conditions in cavity which is rectangular and found that as the viscosity of the vortex increases the average Nusselt number decreases. They found that the circulation strength and the rate of heat transfer of micropolar fluids are lower than Newtonian fluids in similar thermal conditions. Wang and Hsu [20] studied the natural convection micropolar flow in inclined rectangular enclosures, and found that the cavity inclination and the micropolar parameters have a significant influence on the streamline patterns and temperature distribution. They were instrumental in developing understanding of the role of geometry in systems dominated by convection.

Convection problems with internal heated obstacles have also been studied. Rahman et al. [21] have done a finite element analysis of a mixed convection of a heated obstacle in a rectangular cavity. They found that the formation of streamlines and the distribution of temperature is strongly influenced in cavity by the position of the obstacles and the Reynolds number (Re). Mixed convection heat transfer of a heated horizontal square cylinder placed in a square vented cavity was studied by Chamkha, Hussain and Abd-Amer [22]. According to their results, streamline structures, temperature distribution and heat transfer characteristics are significantly influenced by Reynolds number, Richardson number and the location of the obstacles. Numerical investigation within lid driven cavity with mixed convection

flow was performed by Öztop and Dağtekin [23] and it was noticed that with increasing Reynolds number Re, the forced convection flow gradually takes over the natural convection flow, and that increasing Grashof number Gr enhances the buoyancy effect and leads to stronger natural convection circulation. Sheremet and Pop [24] have numerically examined the free convection in a cavity with a micropolar fluid. They found that the vortex structures, temperature distribution and heat transfer properties are greatly affected by micropolar parameters. Additionally, the contribution of microrotation effects to fluid circulation is found to be suppressed with less thermal transport in comparison to the classical Newtonian fluids.

Rashad [25] numerically examined mixed convection heat transfer in a cavity with an internal heat source for a micropolar fluid. It was found that the study revealed that the increase in micropolar coupling parameter decreases the fluid circulation and the mean heat transfer rate and enhances the microrotation effect. Selimefendigil and Öztop [26] studied the mixed convection in a lid-driven cavity filled with obstacles of various geometric shapes and claimed that the geometry of the obstacles is important in the formation of the vortex, fluid circulation, development of thermal boundary layers, and overall heat transfer. Heated obstacles are usually square or rectangular in shape, resulting in greater recirculation regions and temperature gradients than circular obstacles, especially at sharp corners.Using the finite element method, Mohebbi [27] numerically analyzed natural convection in a square cavity containing a heated triangular obstacle. The average heat transfer rate was observed to vary significantly depending on the changes in the location of obstacles, which affects the flow structure and thermal field significantly.

Many studies have been carried out in the literature to investigate how the Reynolds number affects the performance of the mixed convection systems. For lower Reynolds numbers the flow behavior is buoyancy driven and hence the flow circulations are of natural convection type. Forced convection effects increase with an increase in Reynolds number, resulting in greater mixing and better heat transfer performance [23]. Basak et al. [28] studied flow induced by mixed convection in a square enclosure and concluded that for an increase in Grashof number, buoyancy

driven circulation increases and the thermal plume development in the cavity is stronger, which leads to the significant variation in heat transfer and flow characteristics. Other investigations were directed towards the influence of Prandtl number on the heat transfer of mixed convection. Khanafer et al. [29] studied buoyancy-driven convection in enclosures and they concluded that fluids with higher Prandtl numbers have smaller thermal boundary layers and higher temperature gradients near heated surfaces, which leads to higher heat transfer rates. Aydin and Pop [30] treated the case of natural convection in a differentially heated enclosures with micropolar fluid in numerical manner. They concluded that the results indicate that the velocity distribution as well as heat transfer characteristics and intensity of microrotations are greatly influenced by the micropolar parameters, especially the material parameter K. It was observed that the fluid circulations were inhibited and the average Nusselt number Nu was decreased with the increase in the micropolar parameter, which resulted in the decrease of the fluid thermal transport in comparison with Newtonian fluids. Waqas et al. [31] extended the work on the study of mixed convection of micropolar fluids to magnetohydrodynamic (MHD) conditions and showed the presence of a magnetic field creates Lorentz forces that act against the fluid motion. This causes fluid velocity to reduce and the heat transfer properties to be greatly altered as a function of increasing magnetic field strength. Porous media effects have been studied in various convection problems due to their frequent application in geothermal systems, thermal insulation and energy storage devices.Recently, micropolar effects on heat transfer processes have been brought to the fore once again through further studies. Sulaiman et al. [32] have shown that the micropolar parameters can have a non-negligible impact on the thermal transport and flow properties and it is still valid to use the micro polar fluid models for more complex engineering systems. Bejan [2] talked about convection in porous media and reported that permeability and porosity have a significant effect on the characteristics of fluid flow and heat transfer. The effect of reducing the permeability is to increase the resistance to flow, decrease buoyancy-driven circulation, and reduce the convective transfer of heat inside the enclosure. Zienkiewicz, Taylor and Zhu [9] pointed out that stabilized finite element methods, adaptive finite element mesh refinement methods and Galerkin

methods offer better numerical stability and accuracy for convection dominated flow problems with complex geometries and coupled nonlinear equations. One of the most popular numerical methods for numerical analysis of convection-diffusion and fluid flow problems is the Finite Element Method, which is known for its numerical accuracy, flexibility and ability to treat coupled governing equations and complex geometries [9], [33]. The advantage of using FEM is especially useful for solving coupled non-linear equations in irregular domains. The application of FEM to micropolar fluid flow and heat transfer simulations under different boundary conditions has been achieved by many researchers with success. Because of the efficiency in solving coupled partial differential equations in computational fluid dynamics (CFD) research by means of variational formulation, the use of FreeFEM++ has gained popularity.

FreeFEM++ has been successfully applied to incompressible flow simulations, Navier–Stokes equations, heat transfer analysis and micropolar fluid model [13]. Flexible generation of meshes, finite element discretization, implementation of weak forms, the software is perfectly applicable to solving thermal boundary value problems in irregular domains. Recent advances in finite element formulations have improved the numerical simulation of coupled thermo-fluid problems.
Sahoo and Rathish Kumar [34] developed a stabilized finite element framework for mixed convection problems and demonstrated enhanced numerical stability and accuracy for convection dominated flows in complex geometries.

Although, mixed convection and micropolar fluid flow has been extensively studied in literature, not much attention has been paid to the thermal boundary value problems inside square geometries for detailed finite element formulations implemented in FreeFEM++. Thus, further research is needed for a deeper insight into the behavior of thermal transport under the combined effect of obstacle heating, microrotation, buoyancy forces, and forced convection. In recent years, some research has been devoted to understanding micropolar convection, MHD effects, and more complex finite element (FE) formulations, but comparatively little work has been done on detailed finite element implementations of mixed convection of micropolar fluids in square cavities.

1.3 Thesis Contribution

The contributions of this thesis are listed as follows.

This thesis develops a finite element framework for the numerical simulation of transient mixed convection micropolar fluid flow coupled with heat transfer in a two-dimensional enclosure. The governing equations describing continuity, momentum, microrotation, and thermal transport are systematically transformed into their weak (variational) formulations using the Galerkin weighted residual method. The resulting finite element formulation is discretized in time using the implicit backward Euler scheme and successfully implemented in `FreeFEM++` to obtain stable and accurate numerical solutions.

The developed numerical methodology is validated by solving cavity problem and comparing the computed velocity profiles with the benchmark solutions of Ghia *et al.* [35], demonstrating excellent agreement and thereby verifying the correctness of the finite element implementation.

A comprehensive parametric investigation is carried out to examine the influence of the Reynolds number, Prandtl number, micropolar coupling parameter, and Eringen parameter on the velocity, microrotation, and temperature fields. The study provides a detailed physical interpretation of the interactions between translational and rotational motions in micropolar fluids and illustrates how these dimensionless parameters govern momentum transport, thermal diffusion, and angular velocity distributions within the enclosure.

The numerical results, including contour plots and quantitative analyses at selected monitoring locations, provide useful benchmark data for transient mixed convection micropolar flow problems. Furthermore, the developed finite element implementation in `FreeFEM++` establishes a computational framework that can readily be extended to investigate more complex transport phenomena involving magnetic fields, porous media, nanofluids, thermal radiation, or chemically reactive flows.

1.4 Thesis Objectives

The main objectives of this research work are as follows:

i. To formulate the governing equations for transient mixed convection micropolar fluid flow with heat transfer in a two-dimensional enclosure.

ii. To derive the weak (variational) formulation of the governing equations using the Galerkin finite element method.

iii. To develop and implement a finite element algorithm in `FreeFEM++` using the implicit backward Euler time-stepping scheme.

iv. To validate the developed numerical model by comparing the computed results with the benchmark solutions of Ghia *et al.* [35].

v. To investigate the influence of the Reynolds number (Re), Grashof number (Gr), Prandtl number (Pr), micropolar coupling parameter (K), and Eringen parameter (Er) on the velocity, microrotation, and temperature distributions.

vi. To analyze the coupled effects of fluid motion, microrotation and heat transfer through contour plots and quantitative comparisons at selected locations.

vii. To provide physical insights into the influence of micropolar fluid parameters on mixed convection heat transfer and establish a computational framework for future extensions to more complex multiphysics problems.

1.5 Thesis Layout

The thesis is structured into the following chapters:

Chapter 2: Illustrate a brief introduction to the finite element method. This chapter gives an overview of the fundamental concepts of FEM for numerical analysis of mixed convection micropolar flow in a rectangular domain containing heated obstacles. It starts with an introduction to FEM, the discretization of the computational domain, mesh generation and the Galerkin weighted residual method.rotation. Furthermore, the introduction to FreeFEM++ has been discussed in detail. Its application and advantages are equally crucial to be studied.

Importance of FreeFEM++ for the implementation of finite element scheme is also mentioned in this chapter.

Chapter 3: The mathematical description of the thermal boundary value problem of mixed convection micropolar flow in a square domain is presented in this chapter. Physical model, assumptions and equations of continuity, angular momentum, microrotation are introduced. Appropriate boundary conditions and non-dimensional forms of the governing equations are presented. Moreover, the weak formulation and finite element discretization of the governing equations are also presented in this chapter for numerical implementation. Furthermore, the numerical implementation is carried out by using the finite element method in FreeFEM++, which is used to solve the coupled non-linear system of equations for velocity (u, v) , microrotation(ω) , and temperature (Θ).

Chapter 4: This chapter presents and discusses the numerical results obtained from the finite element implementation in FreeFEM++. The developed numerical model is first validated by comparison with published results to verify its accuracy. Thereafter, the effects of the governing dimensionless parameters, namely the Reynolds number (Re), Grashof number (Gr), coupling parameter (K), Eringen number (Er), and Prandtl number (Pr), on the velocity, temperature, microrotation, streamlines, isotherms, and heat transfer characteristics are investigated and discussed in detail.

Chapter 5: This chapter summarizes the major findings of the present research and presents the overall conclusions drawn from the numerical investigation. The main contributions of the study are highlighted, and recommendations for future research are provided to extend the present work.

Chapter 2

Basics of Finite Element Method

The fundamental concepts of finite element method are discussed in this chapter which form the theoretical foundation for the numerical analysis carried out in this thesis.

The Finite element method is a powerful numerical technique used to find the approximate solution to a wide range of mathematical and engineering problems involving partial differential equations. It is based on weak formation and particularly suited to the solution of complex geometries, coupled system and boundary value problem. For this study, the governing equations for the flow of mixed convection micropolar fluid with heat transfer inside a square geometry are solved by using FEM.

2.1 The Basic concept of Finite Element Method

In order to analyze a physical system, a mathematical model is developed to describe a system . While developing the mathematical model, some assumptions are made for simplification. Finally, the governing mathematical expression that consists of differential equations and given conditions, is developed to illustrate the behavior of a system. These differential equations are very difficult to obtain the solutions but it can be possible with the advent of high performance computers.

Various numerical solution techniques have been developed in order to solve

numerous problems. For instance, Micropolar fluid theory introduces additional microrotational effects into classical fluid model, resulting in a coupled system of momentum, angular momentum and energy equations. Due to its non-linear and coupled nature, analytical solutions become difficult to obtain for practical problems. Therefore, numerical methods in particular, the finite element method has been one of the major numerical solution technique for solving such governing equations.

One of the major advantage of FEM is that a general purpose computer program can be developed easily to analyze various kinds of problems. In particular, any complex shape of problem domain with the given conditions can be handled easily by FEM. The FEM requires to partition the computational region into smaller parts called a finite elements. Therefore, the problem domain consists of finite element patches. Each element is solved for in terms of simple polynomial functions known as shape function.All elements are pieced together to get an approximate solution all over the domain. The approach simplifies a continuous problem to a set of discrete algebraic equations that can be solved numerically.

2.1.1 Discretization of the Domain

The domain is subdivided into finite number of elements usually triangular or quadrilateral in two dimensions. The set of elements is called a mesh. Let Ω represent the domain. Then

$$\Omega = \bigcup_{e} \Omega_e, \tag{2.1}$$

where Ω_e represents an individual element. The nodes are where the unknown variables are calculated and each elements are connected at nodes.

2.1.2 Approximation of Field Variables

In FEM, the unknown variables such as velocity (u, v), pressure (p), temperature (θ) and microrotation (ω) are approximated to be:

$$
\begin{aligned}
U^e &\approx \sum_{j=1}^{n} N_j u_j^e, \qquad V^e \approx \sum_{j=1}^{n} N_j v_j^e, \\
W^e &\approx \sum_{j=1}^{n} N_j w_j^e, \qquad P^e \approx \sum_{j=1}^{n} N_j p_j^e, \\
\theta^e &\approx \sum_{j=1}^{n} N_j \theta_j^e
\end{aligned} \tag{2.2}
$$

In which N_j are taken as shape functions, U_j, V_j, W_j, P_j, θ_j are nodal values and n represents the total number of nodes in an element. The same approximation is applied in the governing equation for the dependent variables.

2.1.3 The Method of Weighted Residual

The weighted residual method is used for Finite element formation. The approximate solution is plugged into the governing equations, with a result being residual. This residual can be reduce by imposing:

$$\int_{\Omega} R \cdot W d\Omega = 0, \tag{2.3}$$

It provides a systematic way to drive element equation.

Example 2.1. [36]
To illustrate weighted residual method, consider

$$\frac{\partial^2 u}{\partial x^2} - u = -x, \qquad 0 < x < 1 \tag{2.4}$$

subjected to

$$u(0) = 0, \quad \text{and} \quad u(1) = 0. \tag{2.5}$$

Solution For the approximation to u, assume a trail function u let us suppose a trail function

$$\tilde{u} = ax(1 - x), \tag{2.6}$$

as it must satisfies the BC's and the accuracy of an approximated solution is

dependent upon the selection of the trail function. After that, the residual is computed by using Eq. 2.4 and Eq. 2.6.

$$R = \frac{\partial^2 \tilde{u}}{\partial x^2} - \tilde{u} + x = -2a - ax(1-x) + x, \tag{2.7}$$

because $\tilde{u} \approx u$ and $\tilde{u} \neq u$. Therefore, Eq.2.7 will not vanish. Next is to determine a so that $\tilde{u} \approx u$. For that purpose a test function w is chosen and multiply it with residual Eq.2.7 and integrate the resultant over the domain.

That implies,

$$\begin{aligned} I &= \int_0^1 wR\,dx = \int_0^1 w\left(\frac{\partial^2 \tilde{u}}{\partial x^2} - \tilde{u} + x\right) dx \\ &= \int_0^1 w\left(-2a - ax(1-x) + x\right) dx = 0. \end{aligned} \tag{2.8}$$

Next is to determine the test function w. The methods of weighted residual can be classified on the bases of how the test function is to be determined.

i Collocation Method, In collocation method the test function is taken as $w = \delta(x - x_i)$ where, δ is the Dirac Delta function and x_i are chosen as $0 < x_i < 1$. Let $x_i = 0.5$, then

$$w = \delta(x - 0.5), \tag{2.9}$$

using Eq. 2.8 and Eq. 2.9,

$$I = \int_0^1 (x - 0.5)(-2a - ax(1-x) + x)\,dx = 0,$$

which implies $a = 0.2222$. Then the approximate solution Eq.2.6 becomes,

$$\tilde{u} = 0.2222x(1-x). \tag{2.10}$$

ii Least square method, Here test function is taken as:

$$w = \frac{\partial R}{\partial a}, \tag{2.11}$$

using Eq.2.11 in Eq.2.7

$$w = -2 - x(1 - x),$$

using it in Eq.2.8, gives $a = 0.2305$. Then the approximate solution becomes,

$$\tilde{u} = 0.2305x(1 - x). \tag{2.12}$$

iii Galerkin's method, Here the test function is taken as:

$$w = \frac{\partial \tilde{u}}{\partial a}, \tag{2.13}$$

which implies $w = x(1 - x)$, using in Eq.2.8, gives $a = 0.22272$. Then approximation solution becomes,

$$\tilde{u} = 0.22272x(1 - x). \tag{2.14}$$

2.1.4 Galerkin Finite Element Formation

The Galerkin method is used, where the weighting functions are chosen same as the shape functions. The approach simplifies implementation and ensures consistency of the formulation.

$$w = u(x, y) = \sum N_i(x, y)u_i, \tag{2.15}$$

where,

i $N_i(x, y)$ represents the nodal shape functions,

ii u_i are the unknown nodal values at the i^{th} nodes (e.g., temperatures or velocities at the i^{th} nodes),

iii n represents the total number of nodes per element.

For example: in a linear triangular element case the shape functions would be approximated as:

$$u(x, y) = N_1(x, y)u_1 + N_2(x, y)u_2 + N_3(x, y)u_3,$$

where, $N_1(x, y), N_2(x, y), N_3(x, y)$, are the linear shape functions associated with the three nodes of the triangle.

2.1.5 Weak Formulation

Governing differential equations are transformed into weak (variational) form. This is achieved by:

i Multiplication of equation with a test function.

ii Integrating over a domain.

iii Reducing the order of derivative by using by part integration.

iv This process reduces continuity requirements and automatically puts in boundary conditions in the weak form.

2.1.6 Element Matrices

The weak formation and discretization leads to a system in the form of matrix:

$$[M]^e \frac{\partial U}{\partial t} + [K]^e U + [N]^e U = F^e \tag{2.16}$$

where:
$[M]$ = mass matrix.
$[K]$ = diffusion (stiffness) matrix.
$[N]$ = convection matrix.
$[F]$ = force source matrix. Each element matrix is described below:

The **mass matrix** represents the contribution associated with the time-dependent term of the governing equation. The element mass matrix is defined as:

$$M_{ij}^{(e)} = \int_{\Omega_e} N_i N_j \, d\Omega. \tag{2.17}$$

where N_i and N_j are the shape functions corresponding to the i-th and j-th nodes of the element.

The **diffusion (stiffness) matrix** represents the contribution arising from the diffusion terms in the governing equation. The element stiffness matrix is given by

$$K_{ij}^{(e)} = \int_{\Omega_e} \left(\frac{\partial N_i}{\partial x} \frac{\partial N_j}{\partial x} + \frac{\partial N_i}{\partial y} \frac{\partial N_j}{\partial y} \right) d\Omega. \tag{2.18}$$

The **convection matrix** represents the contribution of the convective terms associated with the fluid velocity. Its element matrix is given by

$$N_{ij}^{(e)} = \int_{\Omega_e} N_i \left(u \frac{\partial N_j}{\partial x} + v \frac{\partial N_j}{\partial y} \right) d\Omega, \tag{2.19}$$

where u and v are the velocity components in the x and y directions, respectively.The **force/source vector** represents the contribution of the source terms and the natural boundary conditions. Its element form is

$$F_i^{(e)} = \int_{\Omega_e} N_i f \, d\Omega + \int_{\Gamma_e} N_i \bar{q} \, d\Gamma, \tag{2.20}$$

where f denotes the source term and $\bar{q}$ represents the prescribed natural boundary condition. At each element, these matrices are calculated and then assembled into global system.

2.1.7 Assembly Process

Connectivity relationships are used to form global system of equations by combining together the element matrices. This process is known as assembly and whole computational domain is referred as the global system.

2.1.8 Boundary Conditions

To obtain a unique solution of a boundary value problem, appropriate boundary conditions must be specified. In the finite element method (FEM), these boundary conditions are imposed into the global algebraic system during its assembly. For a

general boundary value problem, the boundary Γ is divided into two parts as:

$$\Gamma = \Gamma_D \cup \Gamma_N, \tag{2.21}$$

where, Γ_D represents the portion of the boundary on which Dirichlet boundary conditions are prescribed, while Γ_N represents the portion on which Neumann boundary conditions are prescribed. The most common boundary conditions used in fluid flow and heat transfer problems are Dirichlet and Neumann boundary conditions.

i. Dirichlet boundary condition: The Dirichlet boundary condition specifies the value of the dependent variable directly on the boundary and is expressed as:

$$u = \bar{u} \qquad \text{on } \Gamma_D, \tag{2.22}$$

where $\bar{u}$ is the prescribed value of the dependent variable. In FEM, the Dirichlet condition is implemented by directly assigning the prescribed value to the corresponding boundary nodal degree of freedom.

ii. Neumann boundary condition:The Neumann boundary condition specifies the normal derivative or flux of the dependent variable on the boundary and is expressed as:

$$\frac{\partial u}{\partial n} = \bar{q} \qquad \text{on } \Gamma_N, \tag{2.23}$$

where, $\bar{q}$ denotes the prescribed normal derivative or flux. In the weak formulation, Neumann boundary condition appears as a boundary integral and contributes to element force vector as

$$F_i^{(e)} = \int_{\Gamma_N \cap \partial\Omega_e} N_i \bar{q}\, d\Gamma. \tag{2.24}$$

Thus, Dirichlet boundary conditions are imposed directly on corresponding nodal values, whereas Neumann boundary conditions are incorporated through the boundary contribution to finite element force vector.

2.1.9 Solution of Algebraic System

A set of equations is set up and solved numerically. Iterative procedure is used when solving nonlinear problems until convergence.

2.1.10 Advantages of FEM

i. Works well with intricate shapes.

ii. Works well with complex PDEs using coupled variables.

iii. Smooth and adaptable mesh refinement.

iv. If the initial boundary conditions are correct, the computed curve is accurate.

2.1.11 Worked Example: Nonlinear Convection Diffusion Equation

To illustrate the finite element formulation and the assembly procedure discussed in the preceding sections, a one-dimensional nonlinear convection diffusion boundary value problem is considered. The example demonstrates the complete procedure from the strong form of the governing equation to the formation of the global nonlinear algebraic system. Consider the nonlinear convection diffusion equation

$$-\frac{d^2u}{dx^2} + u\frac{du}{dx} = 1, \qquad 0 < x < 1, \tag{2.25}$$

subject to the homogeneous Dirichlet boundary conditions

$$u(0) = 0, \qquad u(1) = 0. \tag{2.26}$$

Here, the first term represents the diffusion contribution, while the second term represents the nonlinear convection contribution.

2.1.11.1 Weak Formulation

Let v be a suitable test function satisfying,

$$v(0) = v(1) = 0. \tag{2.27}$$

Multiplying Eq. (2.25) by the test function v and integrating over the domain gives

$$\int_0^1 \left(-\frac{d^2u}{dx^2} + u\frac{du}{dx} \right) v dx = \int_0^1 v dx. \tag{2.28}$$

Using integration by parts for the second order derivative term gives,

$$\int_0^1 \frac{du}{dx}\frac{dv}{dx}, dx + \int_0^1 u\frac{du}{dx}v, dx = \int_0^1 v, dx. \tag{2.29}$$

The boundary term resulting from integration by parts vanishes because of the prescribed Dirichlet boundary conditions.

Equation (2.29) represents the weak formulation of the nonlinear convection diffusion problem.

2.1.11.2 Finite Element Discretization

The domain is divided into two linear finite elements with three nodes:

$$x_1 = 0, \qquad x_2 = \frac{1}{2}, \qquad x_3 = 1. \tag{2.30}$$

Thus, the element length is

$$h = \frac{1}{2}. \tag{2.31}$$

For a one-dimensional linear element containing $N = 2$ nodes, the approximate solution is expressed as

$$U^h(x) = \sum_{i=1}^{N} N_i(x) U_i, \tag{2.32}$$

where N_i denotes the shape function associated with node i, and U_i represents the corresponding nodal value of the unknown u. In matrix form, the finite element

approximation can be written as:

$$U^h = \mathbf{N}\mathbf{U}^{(e)}, \tag{2.33}$$

where

$$\mathbf{N} = \begin{bmatrix} N_1 & N_2 \end{bmatrix}, \qquad \mathbf{U}^{(e)} = \begin{bmatrix} U_1 \; U_2 \end{bmatrix}. \tag{2.34}$$

For an element extending from x_a to x_b, the linear shape functions are

$$N_1(x) = \frac{x_b - x}{h}, \qquad N_2(x) = \frac{x - x_a}{h}, \tag{2.35}$$

where,

$$h = x_b - x_a. \tag{2.36}$$

Their derivatives are

$$\frac{dN_1}{dx} = -\frac{1}{h}, \qquad \frac{dN_2}{dx} = \frac{1}{h}. \tag{2.37}$$

The derivative of the approximate solution is therefore,

$$\frac{dU^h}{dx} = \sum_{i=1}^{N} \frac{dN_i}{dx} U_i. \tag{2.38}$$

2.1.11.3 Element Matrices and Force Vector

Putting finite element approximations into weak formulation gives element equation

$$K^{(e)}\mathbf{U}^{(e)} + C^{(e)}(\mathbf{U}^{(e)})\mathbf{U}^{(e)} = F^{(e)}, \tag{2.39}$$

where $K^{(e)}$ is element stiffness matrix, $C^{(e)}$ represents nonlinear convection matrix, and $F^{(e)}$ is element force vector. For a transient problem, corresponding mass matrix $M^{(e)}$ would also appear, giving

$$M^{(e)}\dot{\mathbf{U}}^{(e)} + K^{(e)}\mathbf{U}^{(e)} + C^{(e)}(\mathbf{U}^{(e)})\mathbf{U}^{(e)} = F^{(e)}. \tag{2.40}$$

For the present steady state example, the time dependent term is absent.

2.1.11.4 Element Stiffness Matrix

The element stiffness matrix is obtained from the diffusion term as

$$K_{ij}^{(e)} = \int_{x_a}^{x_b} \frac{dN_i}{dx}\frac{dN_j}{dx}, dx, \qquad i,j = 1,\ldots,N. \tag{2.41}$$

For the linear element, this gives

$$K^{(e)} = \frac{1}{h}\begin{bmatrix} 1 & -1 & -1 & 1 \end{bmatrix}. \tag{2.42}$$

Since $h = 1/2$,

$$K^{(e)} = \begin{bmatrix} 2 & -2 & -2 & 2 \end{bmatrix}. \tag{2.43}$$

2.1.11.5 Nonlinear Convection Matrix

The nonlinear convection contribution is obtained from

$$\int_{x_a}^{x_b} U^h \frac{dU^h}{dx} N_i, dx. \tag{2.44}$$

Using

$$U^h = \mathbf{N}\mathbf{U}^{(e)}, \tag{2.45}$$

The nonlinear convection contribution can be expressed in matrix form as:

$$C^{(e)}(\mathbf{U}^{(e)})\mathbf{U}^{(e)} = \int_{x_a}^{x_b} \mathbf{N}^T \left(\mathbf{N}\mathbf{U}^{(e)}\right) \mathbf{B}\mathbf{U}^{(e)}, dx, \tag{2.46}$$

where,

$$\mathbf{B} = \begin{bmatrix} \frac{dN_1}{dx}, \frac{dN_2}{dx} \end{bmatrix}. \tag{2.47}$$

Because the convection term contains the unknown U, the convection matrix depends on the current nodal solution. Therefore, it is denoted by

$$C^{(e)} = C^{(e)}(\mathbf{U}^{(e)}). \tag{2.48}$$

This dependence makes the resulting finite element system nonlinear.

2.1.11.6 Element Force Vector

The element force vector is obtained from the right-hand side of Eq. (2.29):

$$F_i^{(e)} = \int_{x_a}^{x_b} N_i, dx. \tag{2.49}$$

Thus,

$$F^{(e)} = \left[\int_{x_a}^{x_b} N_1, dx, \int_{x_a}^{x_b} N_2, dx \right]. \tag{2.50}$$

For linear shape functions,

$$F^{(e)} = \frac{h}{2} \left[1 \; 1 \right]. \tag{2.51}$$

Since $h = 1/2$,

$$F^{(e)} = \left[1/4 \; 1/4 \right]. \tag{2.52}$$

2.1.11.7 Assembly of the Global System

The two elements are connected through the common node x_2. The element matrices and force vectors are assembled according to their corresponding global node numbers. The global stiffness matrix obtained from Eq. (2.43) is

$$K = \begin{bmatrix} 2 & -2 & 0 & -2 & 4 & -2 & 0 & -2 & 2 \end{bmatrix}. \tag{2.53}$$

Similarly, the global force vector is

$$F = \left[1/4 \; 1/2 \; 1/4 \right]. \tag{2.54}$$

Consequently, the global nonlinear finite element system takes the form:

$$K\mathbf{U} + C(\mathbf{U})\mathbf{U} = F, \tag{2.55}$$

where,

$$\mathbf{U} = \left[U_1 \; U_2 \; U_3 \right]. \tag{2.56}$$

Equation (2.55) demonstrates that the global system cannot be solved directly as a conventional linear system because the convection matrix depends on the unknown solution.

2.1.11.8 Application of Boundary Conditions

The prescribed boundary conditions are

$$u_1 = 0, \qquad u_3 = 0. \tag{2.57}$$

After applying these conditions, only the interior nodal value u_2 remains unknown. The resulting nonlinear algebraic equation can be represented in the form,

$$R(u_2) = 0, \tag{2.58}$$

where R denotes the nonlinear residual. The nonlinear equation can be solved iteratively using, for example, the Newton Raphson method. The general Newton iteration is written as

$$U_2^{(k+1)} = U_2^{(k)} \frac{R(U_2^{(k)})}{R'(U_2^{(k)})}. \tag{2.59}$$

The iteration is continued until the convergence criterion,

$$\left| U_2^{(k+1)} - U_2^{(k)} \right| < \varepsilon \tag{2.60}$$

is satisfied, where ε is a prescribed tolerance.

2.1.11.9 Summary of the Worked Example

The above example illustrates the complete finite element procedure for a nonlinear convection diffusion equation. The governing differential equation is first transformed into its weak form. The approximate solution is then represented in terms of the shape functions N_i and the nodal values U_i. The element stiffness matrix $K^{(e)}$, nonlinear convection matrix $M^{(e)}(\mathbf{U}^{(e)})$, and force vector $F^{(e)}$ are subsequently constructed. These element level quantities are assembled to form the global nonlinear algebraic system. The example demonstrates the general

procedure that is also followed for the more complex coupled governing equations considered in the present study. In the mathematical model presented in the next chapter, the same finite element concepts are extended to the coupled velocity, pressure, temperature, and microrotational fields.

2.2 Introduction to FreeFEM++

FreeFEM++ is an open source, high level programming language numerical software for solving partial differential equations (PDEs) by the Finite element method (FEM). It offers a intuitive syntax for creating meshes, defining intricate geometry and running numerical simulations.

2.2.1 Formation of FreeFEM++

In FreeFEM++, a formation refers to the weak form of Partial Differential Equation that is solved using FEM. The standard way to define a formulation in FreeFEM++ is through the variational formation or more structured formation.

2.2.2 Significance of FreeFEM++

i It offers a versatile and efficient framework to enable the development of variational formations and to solve complicated engineering and scientific problems involving fluid flow, heat transfer, structural analysis and multi-physics systems and in applied mathematics.

ii It offers a straight forward and adaptable scripting language, in contrast to many FEM solvers that necessitate substantial code.Because of this, both novice and seasoned researchers can use it.

iii It has ability to solve complex coupled PDEs with relatively simple coding, efficiently.

iv It also supports built-in mesh generation, visualization tools, and adaptive refinement techniques using a high level programming language specially written for finite element computations to improve accuracy and efficiency.

v It is able to work with different finite element spaces and numerical solvers and can therefore be used to solve both steady and time dependent problems.

vi Because of its versatility, robustness, and excellent finite element capabilities, the use of FreeFEM++ in computational field and heat dynamics research has increased dramatically.

2.2.3 Advantages of Using FreeFEM++

i User friendly: Quick prototyping with an easy to understand and adaptable syntax.

ii Strong: Integrated solvers and sophisticated FEM capabilities.

iii Effective: Enhanced functionality for extensive simulation.

iv Community support: A vibrant user base and extensive documentation.

2.2.3.1 FreeFEM++ Implementation Algorithm

The nonlinear convection diffusion problem is implemented in FreeFEM++ using the finite element formulation developed above. The nonlinear convection term is treated iteratively by using the solution from the previous iteration. The computational procedure is summarized as follows:

i Define the one-dimensional computational domain $0 \leq x \leq 1$ and generate the finite element mesh.

ii Define the linear finite element space using P_1 elements.

iii Define the unknown solution u and the test function v.

iv Initialize the solution $u^{(0)}$.

v Use the previous iteration solution $u^{(k)}$ in the nonlinear convection term

$$u\frac{du}{dx}.$$

vi Assemble the diffusion and convection contributions together with the force vector corresponding to the source term $f = 1$.

vii Impose the homogeneous Dirichlet boundary conditions

$$u(0) = u(1) = 0.$$

viii Solve the resulting linearized finite element system to obtain $u^{(k+1)}$.

ix Evaluate the difference between two successive solutions.

x Repeat the iteration.

xi The converged solution is taken as the numerical solution of the nonlinear convection diffusion problem.

Chapter 3

Mathematical Equations

3.1 Physical Description of the Problem:

The physical model studied in this paper is the two dimensional square cavity containing an incompressible micropolar fluid. The cavity is centered on the origin of the Cartesian coordinate system. The symbols X and Y represent horizontal and vertical coordinates respectively. The computational domain is surrounded by four walls at:

$$-0.5 \leq X \leq 0.5, \qquad -0.5 \leq Y \leq 0.5,$$

The top and bottom surfaces of the cavity are T_1 and B_1, respectively. The wall on the left is subdivided into three parts: L_1 , L_2 and L_3 and the wall on the right is subdivided into three parts: R_1 and R_2 and R_3. The fluid enters the cavity through inlet L_1 and exists through the outlet R_1, that is producing forced convectionof the flow. The wall L_3 is heated, creating a temperature difference within cavity that generates buoyancy forces. The simultaneous effect of forced and natural convection results in mixed convection. The remaining boundar sections are subjected to the conditions specified in the mathematical model.

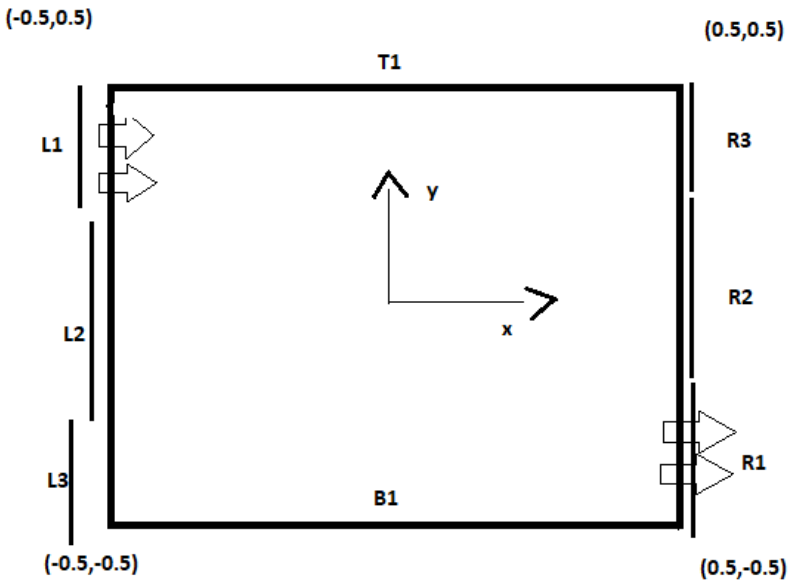


FIGURE 3.1: Schematic representation of the computational domain and boundary configuration.

Figure 3.1 shows the computational domain, coordinate system, and boundary segments used in the present investigation.

3.2 Mathematical Model

The flow is assumed to be two-dimensional, incompressible, laminar and unsteady, based on the physical configuration shown in Figure 3.1. The chamber is filled with a micropolar fluid and the heat transfer is done by mixed convection, considering the effect of both buoyancy and forced flow. The properties of the fluids are assumed to be constant except for the change in density in the buoyancy term that is modeled with the Boussinesq approximation. Based on these assumptions, the conservation of mass, linear momentum, angular momentum and energy equations describe the fluid flow and heat transfer within the cavity.

3.2.1 Governing Equations in Dimensional Form

The dimensional form of the continuity, momentum, microrotation and energy equations for the proposed problem are given below:

Continuity Equation:

$$\frac{\partial u}{\partial x}+\frac{\partial v}{\partial y}=0. \tag{3.1}$$

Momentum equation for u-velocity

$$\frac{\partial u}{\partial t}+u\frac{\partial u}{\partial x}+v\frac{\partial u}{\partial y}=-\frac{1}{\rho}\frac{\partial p}{\partial x}+\frac{\mu}{\rho}\left(\frac{\partial^2 u}{\partial x^2}+\frac{\partial^2 u}{\partial y^2}\right)+\frac{\kappa}{\rho}\left(\frac{\partial w}{\partial y}\right). \tag{3.2}$$

Momentum equation for v-velocity

$$\frac{\partial v}{\partial t}+u\frac{\partial v}{\partial x}+v\frac{\partial v}{\partial y}=-\frac{1}{\rho}\frac{\partial p}{\partial y}+\frac{\mu}{\rho}\left(\frac{\partial^2 v}{\partial x^2}+\frac{\partial^2 v}{\partial y^2}\right)-\frac{\kappa}{\rho}\left(\frac{\partial w}{\partial x}\right)+g\beta(\Theta-\Theta_c). \tag{3.3}$$

Micro-rotational equation

$$\frac{\partial \omega}{\partial t}+u\frac{\partial \omega}{\partial x}+v\frac{\partial \omega}{\partial y}=\frac{\gamma}{\rho j}\left(\frac{\partial^2 \omega}{\partial x^2}+\frac{\partial^2 \omega}{\partial y^2}\right)+\frac{2\kappa}{\rho j}\left(\frac{\partial v}{\partial x}-\frac{\partial u}{\partial y}-2\omega\right). \tag{3.4}$$

Energy equation

$$\frac{\partial \Theta}{\partial t}+u\frac{\partial \Theta}{\partial x}+v\frac{\partial \Theta}{\partial y}=\alpha\left(\frac{\partial^2 \Theta}{\partial x^2}+\frac{\partial^2 \Theta}{\partial y^2}\right). \tag{3.5}$$

These equations subject to the following boundary conditions.

At Left:

$$on \quad L1: \quad u=U_0=1, \quad v=0, \quad \omega=0,$$

$$on \quad L2: \quad u=0, \quad v=0, \quad \omega=0,$$

$$on \quad L3: \quad u=0, \quad v=0, \quad \omega=0, \quad \Theta=\Theta_h=100.$$

At Right:

$$on \quad R1: \quad \frac{\partial u}{\partial x}=0, \quad \frac{\partial v}{\partial x}=0, \quad \frac{\partial \omega}{\partial x}=0, \quad \frac{\partial \Theta}{\partial x}=0.$$

$$on \quad R2: \quad u=0, \quad v=0, \quad \omega=0, \quad \frac{\partial \Theta}{\partial x}=0.$$

$$on \quad R3: \quad u=0, \quad v=0, \quad \omega=0,$$

At Top:

$$u = 0, \quad v = 0, \quad \omega = 0, \quad \frac{\partial \Theta}{\partial y} = 0,$$

At Bottom:

$$u = 0, \quad v = 0, \quad \omega = 0, \quad \frac{\partial \Theta}{\partial y} = 0,$$

Dimensionless Parameters

The following dimensionless variables are introduced to convert the dimensional governing equations into non-dimensional form.

$$X = \frac{x}{L}, \quad Y = \frac{y}{L}, \quad U = \frac{u}{U_0}, \quad V = \frac{v}{U_0}, \quad T = \frac{tU_o}{L},$$

$$W = \frac{L\omega}{U_o}, \quad P = \frac{p}{\rho U_0^2}, \quad \theta = \frac{\Theta - \Theta_c}{\Theta_h - \Theta_c}.$$

3.2.2 Conversion of Dimensional Form into Dimension-less Form

In order to transform the governing system of equations Eq.3.1-Eq.3.5 into dimensionless form of partial differential equations, the following provides detailed calculations of the different differential terms arising in the governing system.

$$X = \frac{x}{L} \quad \Rightarrow \quad \frac{\partial X}{\partial x} = \frac{1}{L},$$

$$Y = \frac{y}{L} \quad \Rightarrow \quad \frac{\partial Y}{\partial y} = \frac{1}{L},$$

$$U = \frac{u}{u_o} \quad \Rightarrow \quad u = u_o U,$$

$$V = \frac{v}{u_o} \quad \Rightarrow \quad v = u_o V,$$

$$W = \frac{L\omega}{u_0} \quad \Rightarrow \quad \omega = \frac{W u_0}{L},$$

$$P = \frac{p}{\rho u_0^2} \quad \Rightarrow \quad p = P\rho u_0^2,$$

$$T = \frac{u_o}{L}t \quad \Rightarrow \quad \frac{\partial T}{\partial t} = \frac{u_o}{L},$$

$$\theta = \frac{\Theta - \Theta_c}{\Theta_h - \Theta_c} \quad \Rightarrow \quad \Theta = \Theta_c + (\Theta_h - \Theta_c)\theta,$$

$$\frac{\partial u}{\partial t} = \frac{\partial u}{\partial T}\frac{\partial T}{\partial t} = \frac{\partial}{\partial T}(u)\frac{\partial}{\partial t}(T) = \frac{\partial}{\partial T}(u_o U)\frac{u_o}{L} = u_o\frac{\partial U}{\partial T}\frac{u_o}{L} = \frac{u_o^2}{L}\frac{\partial U}{\partial T},$$

$$\frac{\partial u}{\partial x} = \frac{\partial u}{\partial X}\frac{\partial X}{\partial x} = \frac{\partial}{\partial X}(u)\frac{1}{L} = \frac{\partial}{\partial X}(u_o U)\frac{1}{L} = \frac{u_o}{L}\frac{\partial U}{\partial X},$$

$$\frac{\partial u}{\partial y} = \frac{\partial u}{\partial Y}\frac{\partial Y}{\partial y} = \frac{\partial}{\partial Y}(u)\frac{1}{L} = \frac{\partial}{\partial Y}(u_o U)\frac{1}{L} = \frac{u_o}{L}\frac{\partial U}{\partial Y},$$

$$u\frac{\partial u}{\partial x} = u_o U\frac{u_o}{L}\frac{\partial U}{\partial X} = \frac{u_o^2}{L}U\frac{\partial U}{\partial X},$$

$$v\frac{\partial u}{\partial y} = u_o V\frac{u_o}{L}\frac{\partial U}{\partial Y} = \frac{u_o^2}{L}V\frac{\partial U}{\partial Y},$$

$$\frac{\partial p}{\partial x} = \frac{\partial p}{\partial X}\frac{\partial X}{\partial x} = \frac{\partial}{\partial X}(P\rho u_0^2)\frac{1}{L} = \frac{\rho u_o^2}{L}\frac{\partial P}{\partial X},$$

$$-\frac{1}{\rho}\frac{\partial p}{\partial x} = -\frac{1}{\rho}\frac{\rho u_o^2}{L}\frac{\partial P}{\partial X} = -\frac{u_o^2}{L}\frac{\partial P}{\partial X},$$

$$\frac{\partial^2 u}{\partial x^2} = \frac{\partial}{\partial x}\left(\frac{\partial u}{\partial x}\right) = \frac{\partial}{\partial x}\left(\frac{u_o}{L}\frac{\partial U}{\partial X}\right) = \frac{\partial}{\partial X}\frac{\partial X}{\partial x}\left(\frac{u_o}{L}\frac{\partial U}{\partial X}\right)$$
$$\Rightarrow \frac{\partial}{\partial X}\frac{1}{L}\left(\frac{u_o}{L}\frac{\partial U}{\partial X}\right) = \frac{u_o}{L^2}\frac{\partial^2 U}{\partial X^2},$$

$$\frac{\mu}{\rho}\frac{\partial^2 u}{\partial x^2} = \frac{\mu}{\rho}\frac{u_o}{L^2}\frac{\partial^2 U}{\partial X^2},$$

$$\frac{\partial^2 u}{\partial y^2} = \frac{\partial}{\partial y}\left(\frac{\partial u}{\partial y}\right) = \frac{\partial}{\partial y}\left(\frac{u_o}{L}\frac{\partial U}{\partial Y}\right) = \frac{\partial}{\partial Y}\frac{\partial Y}{\partial y}\left(\frac{u_o}{L}\frac{\partial U}{\partial Y}\right)$$
$$\Rightarrow \frac{\partial}{\partial Y}\frac{1}{L}\left(\frac{u_o}{L}\frac{\partial U}{\partial Y}\right) = \frac{u_o}{L^2}\frac{\partial^2 U}{\partial Y^2},$$

$$\frac{\mu}{\rho}\frac{\partial^2 u}{\partial y^2} = \frac{\mu}{\rho}\frac{u_o}{L^2}\frac{\partial^2 U}{\partial Y^2},$$

$$\frac{\partial v}{\partial t} = \frac{\partial v}{\partial T}\frac{\partial T}{\partial t} = \frac{\partial}{\partial T}(v)\frac{\partial}{\partial t}(T) = \frac{\partial}{\partial T}(u_o V)\frac{u_o}{L} = u_o\frac{\partial V}{\partial T}\frac{u_o}{L} = \frac{u_o^2}{L}\frac{\partial V}{\partial T},$$

$$\frac{\partial v}{\partial x} = \frac{\partial v}{\partial X}\frac{\partial X}{\partial x} = \frac{\partial}{\partial X}(v)\frac{1}{L} = \frac{\partial}{\partial X}(u_o V)\frac{1}{L} = \frac{u_o}{L}\frac{\partial V}{\partial X},$$

$$\frac{\partial v}{\partial y} = \frac{\partial v}{\partial Y}\frac{\partial Y}{\partial y} = \frac{\partial}{\partial Y}(v)\frac{1}{L} = \frac{\partial}{\partial Y}(u_o V)\frac{1}{L} = \frac{u_o}{L}\frac{\partial V}{\partial Y},$$

$$u\frac{\partial v}{\partial x} = (u_0 U)\frac{u_o}{L}\frac{\partial V}{\partial X} = \frac{u_0^2}{L}U\frac{\partial V}{\partial X},$$

$$v\frac{\partial v}{\partial y} = u_o V\frac{u_o}{L}\frac{\partial V}{\partial Y} = \frac{u_o^2}{L}V\frac{\partial V}{\partial Y},$$

$$\frac{\partial p}{\partial y} = \frac{\partial p}{\partial Y}\frac{\partial Y}{\partial y} = \frac{\partial}{\partial Y}(P\rho u_0^2)\frac{1}{L} = \frac{\rho u_o^2}{L}\frac{\partial P}{\partial Y},$$

$$-\frac{1}{\rho}\frac{\partial p}{\partial y} = -\frac{1}{\rho}\frac{\rho u_o^2}{L}\frac{\partial P}{\partial Y} = -\frac{u_o^2}{L}\frac{\partial P}{\partial Y},$$

$$\frac{\partial^2 v}{\partial x^2} = \frac{\partial}{\partial x}\left(\frac{\partial v}{\partial x}\right) = \frac{\partial}{\partial x}\left(\frac{u_o}{L}\frac{\partial V}{\partial X}\right) = \frac{\partial}{\partial X}\frac{\partial X}{\partial x}\left(\frac{u_o}{L}\frac{\partial V}{\partial X}\right)$$
$$\Rightarrow \frac{\partial}{\partial X}\frac{1}{L}\left(\frac{u_o}{L}\frac{\partial V}{\partial X}\right) = \frac{u_o}{L^2}\frac{\partial^2 V}{\partial X^2},$$

$$\frac{\mu}{\rho}\frac{\partial^2 v}{\partial x^2} = \frac{\mu}{\rho}\frac{u_o}{L^2}\frac{\partial^2 V}{\partial X^2},$$

$$\frac{\partial^2 v}{\partial y^2} = \frac{\partial}{\partial y}\left(\frac{\partial v}{\partial y}\right) = \frac{\partial}{\partial y}\left(\frac{u_o}{L}\frac{\partial V}{\partial Y}\right) = \frac{\partial}{\partial Y}\frac{\partial Y}{\partial y}\left(\frac{u_o}{L}\frac{\partial V}{\partial Y}\right)$$
$$\Rightarrow \frac{\partial}{\partial Y}\frac{1}{L}\left(\frac{u_o}{L}\frac{\partial V}{\partial Y}\right) = \frac{\partial^2 v}{\partial y^2} = \frac{u_o}{L^2}\frac{\partial^2 V}{\partial Y^2},$$

$$\frac{\mu}{\rho}\frac{\partial^2 v}{\partial y^2} = \frac{\mu}{\rho}\frac{u_o}{L^2}\frac{\partial^2 V}{\partial Y^2},$$

$$g\beta(\Theta - \Theta_c) = g\beta(\Theta_h - \Theta_c)\theta,$$

$$\frac{\partial \omega}{\partial t} = \frac{\partial \omega}{\partial T}\frac{\partial T}{\partial t} = \frac{\partial}{\partial T}(\omega)\frac{\partial}{\partial t}(T) = \frac{\partial}{\partial T}\left(\frac{u_o W}{L}\right)\frac{u_o}{L} = \frac{u_o^2}{L^2}\frac{\partial W}{\partial T},$$

$$\frac{\partial \omega}{\partial x} = \frac{\partial \omega}{\partial X}\frac{\partial X}{\partial x} = \frac{\partial}{\partial X}(\omega)\frac{1}{L} = \frac{\partial}{\partial X}\left(\frac{u_o W}{L}\right)\frac{1}{L} = \frac{u_o}{L^2}\frac{\partial W}{\partial X},$$

$$\frac{\partial \omega}{\partial y} = \frac{\partial \omega}{\partial Y}\frac{\partial Y}{\partial x} = \frac{\partial}{\partial Y}(\omega)\frac{1}{L} = \frac{\partial}{\partial Y}\left(\frac{u_o W}{L}\right)\frac{1}{L} = \frac{u_o}{L^2}\frac{\partial W}{\partial Y},$$

$$u\frac{\partial \omega}{\partial x} = (u_0 U)\frac{u_o}{L^2}\frac{\partial W}{\partial X} = (U)\frac{u_o^2}{L^2}\frac{\partial W}{\partial X},$$

$$v\frac{\partial \omega}{\partial y} = u_o V\frac{u_o}{L^2}\frac{\partial W}{\partial Y} = \frac{u_o^2}{L^2}V\frac{\partial W}{\partial Y},$$

$$\frac{\partial^2 \omega}{\partial x^2} = \frac{\partial}{\partial x}\left(\frac{\partial \omega}{\partial x}\right) = \frac{\partial}{\partial x}\left(\frac{u_o}{L^2}\frac{\partial W}{\partial X}\right) = \frac{\partial}{\partial X}\frac{\partial X}{\partial x}\left(\frac{u_o}{L^2}\frac{\partial W}{\partial X}\right)$$
$$\Rightarrow \frac{\partial}{\partial X}\frac{1}{L}\left(\frac{u_o}{L^2}\frac{\partial W}{\partial X}\right) = \frac{u_o}{L^3}\frac{\partial^2 W}{\partial X^2},$$

$$\frac{\gamma}{\rho j}\frac{\partial^2 \omega}{\partial x^2} = \frac{\mu}{\rho j}\left(1 + \frac{K}{2}\right)\frac{u_o}{L^3}\frac{\partial^2 W}{\partial x^2},$$

$$\frac{\partial^2\omega}{\partial y^2}=\frac{\partial}{\partial y}\left(\frac{\partial\omega}{\partial y}\right)=\frac{\partial}{\partial y}\left(\frac{u_o}{L^2}\frac{\partial W}{\partial Y}\right)=\frac{\partial}{\partial Y}\frac{\partial Y}{\partial y}\left(\frac{u_o}{L^2}\frac{\partial W}{\partial Y}\right)$$
$$\Rightarrow\frac{\partial}{\partial Y}\frac{1}{L}\left(\frac{u_o}{L^2}\frac{\partial W}{\partial Y}\right)=\frac{u_o}{L^3}\frac{\partial^2 W}{\partial Y^2},$$

$$\frac{\gamma}{\rho j}\frac{\partial^2\omega}{\partial y^2}=\frac{\mu}{\rho j}\left(1+\frac{K}{2}\right)\frac{u_o}{L^3}\frac{\partial^2 W}{\partial Y^2},$$

$$\frac{\kappa}{\rho}\frac{\partial\omega}{\partial y}=\frac{\kappa u_o}{\rho L^2}\frac{\partial W}{\partial Y},$$

$$-\frac{\kappa}{\rho}\frac{\partial\omega}{\partial x}=-\frac{\kappa u_o}{\rho L^2}\frac{\partial W}{\partial X},$$

$$-2\omega=-2\left(\frac{u_0}{L}\right)W=-\frac{2u_0}{L}W,$$

$$\frac{2\kappa}{\rho j}\frac{\partial v}{\partial x}=\frac{2\kappa u_0}{\rho jL}\frac{\partial V}{\partial X},$$

$$\frac{2\kappa}{\rho j}\frac{\partial u}{\partial y}=\frac{2\kappa u_0}{\rho jL}\frac{\partial U}{\partial Y},$$

$$\frac{\partial\Theta}{\partial t}=\frac{\partial\Theta}{\partial T}\frac{\partial T}{\partial t}=\frac{\partial}{\partial T}(\Theta)\frac{\partial}{\partial t}(\,T)=\frac{\partial}{\partial T}(\Theta_c+(\Theta_h-\Theta_c)\theta)\frac{u_o}{L}=(\Theta_h-\Theta_c)\frac{u_o}{L}\frac{\partial\theta}{\partial T},$$

$$\frac{\partial\Theta}{\partial x}=\frac{\partial\Theta}{\partial X}\frac{\partial X}{\partial t}=\frac{\partial}{\partial X}(\Theta)\frac{\partial}{\partial t}(X)=\frac{\partial}{\partial X}(\Theta_c+(\Theta_h-\Theta_c)\theta)\frac{1}{L}=(\Theta_h-\Theta_c)\frac{1}{L}\frac{\partial\theta}{\partial X},$$

$$\frac{\partial\Theta}{\partial y}=\frac{\partial\Theta}{\partial Y}\frac{\partial Y}{\partial t}=\frac{\partial}{\partial Y}(\Theta)\frac{\partial}{\partial t}(Y)=\frac{\partial}{\partial Y}(\Theta_c+(\Theta_h-\Theta_c)\theta)\frac{1}{L}=(\Theta_h-\Theta_c)\frac{1}{L}\frac{\partial\theta}{\partial Y},$$

$$u\frac{\partial\Theta}{\partial x}=(u_0U)(\Theta_h-\Theta_c)\frac{1}{L}\frac{\partial\theta}{\partial X}=(\Theta_h-\Theta_c)U\frac{u_0}{L}\frac{\partial\theta}{\partial X},$$

$$v\frac{\partial\Theta}{\partial y}=(u_0V)(\Theta_h-\Theta_c)\frac{1}{L}\frac{\partial\theta}{\partial Y}=(\Theta_h-\Theta_c)V\frac{u_0}{L}\frac{\partial\theta}{\partial Y},$$

$$\frac{\partial^2\Theta}{\partial x^2}=\frac{\partial}{\partial x}\left(\frac{\partial\Theta}{\partial x}\right)=\frac{\partial}{\partial x}\left((\Theta_h-\Theta_c)\frac{1}{L}\frac{\partial\theta}{\partial X}\right)=\frac{\partial}{\partial X}\frac{\partial X}{\partial x}\left((\Theta_h-\Theta_c)\frac{1}{L}\frac{\partial\theta}{\partial X}\right)$$
$$\Rightarrow\frac{\partial}{\partial X}\frac{1}{L}\left((\Theta_h-\Theta_c)\frac{1}{L}\frac{\partial\theta}{\partial X}\right)=\frac{\Theta_h-\Theta_c}{L^2}\frac{\partial^2\theta}{\partial X^2},$$

$$\alpha\frac{\partial^2\Theta}{\partial x^2}=\frac{\alpha(\Theta_h-\Theta_c)}{L^2}\frac{\partial^2\theta}{\partial X^2},$$

$$\frac{\partial^2\Theta}{\partial y^2}=\frac{\partial}{\partial y}\left(\frac{\partial\Theta}{\partial y}\right)=\frac{\partial}{\partial y}\left((\Theta_h-\Theta_c)\frac{1}{L}\frac{\partial\theta}{\partial Y}\right)=\frac{\partial}{\partial Y}\frac{\partial Y}{\partial y}\left((\Theta_h-\Theta_c)\frac{1}{L}\frac{\partial\theta}{\partial Y}\right)$$
$$\Rightarrow\frac{\partial}{\partial Y}\frac{1}{L}\left((\Theta_h-\Theta_c)\frac{1}{L}\frac{\partial\theta}{\partial Y}\right)=\frac{\Theta_h-\Theta_c}{L^2}\frac{\partial^2\theta}{\partial Y^2},$$

$$\alpha\frac{\partial^2\Theta}{\partial y^2}=\frac{\alpha(\Theta_h-\Theta_c)}{L^2}\frac{\partial^2\theta}{\partial Y^2},$$

Now, the dimensionless form of the continuity equation (3.1) can be obtained as follows,

$$\frac{\partial u}{\partial x}+\frac{\partial v}{\partial y}=0,$$
$$\frac{u_o}{L}\frac{\partial U}{\partial X}+\frac{u_o}{L}\frac{\partial V}{\partial Y}=0,$$
$$\frac{u_o}{L}\left(\frac{\partial U}{\partial X}+\frac{\partial V}{\partial Y}\right)=0,$$

As $\frac{u_o}{L}\neq 0$ but,

$$\frac{\partial U}{\partial X}+\frac{\partial V}{\partial Y}=0. \tag{3.6}$$

The dimensionless form of the u-momentum equation (3.2) can be obtained as follow:

$$\frac{\partial u}{\partial t}+u\frac{\partial u}{\partial x}+v\frac{\partial u}{\partial y}+=-\frac{1}{\rho}\frac{\partial p}{\partial x}+\frac{\mu}{\rho}\left(\frac{\partial^2 u}{\partial x^2}+\frac{\partial^2 u}{\partial y^2}\right)+\frac{\kappa}{\rho}\frac{\partial w}{\partial y},$$
$$\frac{u_o^2}{L}\frac{\partial U}{\partial T}+\frac{u_o^2}{L}U\frac{\partial U}{\partial X}+\frac{u_o^2}{L}V\frac{\partial U}{\partial Y}=-\frac{u_o^2}{L}\frac{\partial P}{\partial X}+\frac{\mu}{\rho}\left(\frac{u_o}{L^2}\frac{\partial^2 U}{\partial X^2}+\frac{u_o}{L^2}\frac{\partial^2 U}{\partial Y^2}\right)+\frac{\kappa u_o}{\rho L^2}\frac{\partial W}{\partial Y},$$
$$\frac{u_o^2}{L}\left[\frac{\partial U}{\partial T}+U\frac{\partial U}{\partial X}+V\frac{\partial U}{\partial Y}\right]=-\frac{u_o^2}{L}\frac{\partial P}{\partial X}+\frac{\mu}{\rho}\frac{u_o}{L^2}\left(\frac{\partial^2 U}{\partial X^2}+\frac{\partial^2 U}{\partial Y^2}\right)+\frac{u_0}{L^2}\frac{\kappa}{\rho}\left(\frac{\partial W}{\partial Y}\right),$$
$$\frac{\partial U}{\partial T}+U\frac{\partial U}{\partial X}+V\frac{\partial U}{\partial Y}=-\frac{\partial P}{\partial X}+\frac{L\mu}{\rho u_o^2}\frac{u_o}{L^2}\left(\frac{\partial^2 U}{\partial X^2}+\frac{\partial^2 U}{\partial Y^2}\right)+\frac{\kappa}{\rho u_o L}\frac{\partial W}{\partial Y},$$
$$\frac{\partial U}{\partial T}+U\frac{\partial U}{\partial X}+V\frac{\partial U}{\partial Y}+=-\frac{\partial P}{\partial X}+\frac{\mu}{L\rho u_o}\left(\frac{\partial^2 U}{\partial X^2}+\frac{\partial^2 U}{\partial Y^2}\right)+\frac{K\mu}{\rho u_o L}\frac{\partial W}{\partial Y},$$
$$\frac{\partial U}{\partial T}+U\frac{\partial U}{\partial X}+V\frac{\partial U}{\partial Y}=-\frac{\partial P}{\partial X}+\frac{1}{\frac{\rho L u_o}{\mu}}\left(\frac{\partial^2 U}{\partial X^2}+\frac{\partial^2 U}{\partial Y^2}\right)+\frac{K}{\frac{\rho L u_o}{\mu}}\frac{\partial W}{\partial Y},$$
$$\frac{\partial U}{\partial T}+U\frac{\partial U}{\partial X}+V\frac{\partial U}{\partial Y}=-\frac{\partial P}{\partial X}+\frac{1}{Re}\left(\frac{\partial^2 U}{\partial X^2}+\frac{\partial^2 U}{\partial Y^2}\right)+\frac{K}{Re}\frac{\partial W}{\partial Y}. \tag{3.7}$$

Similarly, the dimensionless form of the v-momentum equation (3.3) can be obtained as follow:

$$\frac{\partial v}{\partial t}+u\frac{\partial v}{\partial x}+v\frac{\partial v}{\partial y}+=-\frac{1}{\rho}\frac{\partial p}{\partial y}+\frac{\mu}{\rho}\left(\frac{\partial^2 v}{\partial x^2}+\frac{\partial^2 v}{\partial y^2}\right)-\frac{\kappa}{\rho}\frac{\partial w}{\partial x}+g\beta(\Theta-\Theta_c),$$

$$\frac{u_o^2}{L}\frac{\partial V}{\partial T}+\frac{u_o^2}{L}U\frac{\partial V}{\partial X}+\frac{u_o^2}{L}V\frac{\partial V}{\partial Y}$$
$$\Rightarrow -\frac{u_o^2}{L}\frac{\partial P}{\partial Y}+\frac{\mu}{\rho}\left(\frac{u_o}{L^2}\frac{\partial^2 V}{\partial X^2}+\frac{u_o}{L^2}\frac{\partial^2 V}{\partial Y^2}\right)-\frac{\kappa u_o}{\rho L^2}\frac{\partial W}{\partial X}+g\beta(\Theta_h-\Theta_c)\theta,$$

$$\frac{u_o^2}{L}\left[\frac{\partial V}{\partial T}+U\frac{\partial V}{\partial X}+V\frac{\partial V}{\partial Y}\right]$$
$$\Rightarrow -\frac{u_o^2}{L}\frac{\partial P}{\partial Y}+\frac{\mu}{\rho}\frac{u_o}{L^2}\left(\frac{\partial^2 V}{\partial X^2}+\frac{\partial^2 V}{\partial Y^2}\right)-\frac{u_0}{L^2}\frac{\kappa}{\rho}\left(\frac{\partial W}{\partial X}\right)+g\beta(\Theta_h-\Theta_c)\theta,$$

$$\frac{\partial V}{\partial T}+U\frac{\partial V}{\partial X}+V\frac{\partial V}{\partial Y}$$
$$\Rightarrow -\frac{\partial P}{\partial Y}+\frac{L\mu}{\rho u_o^2}\frac{u_o}{L^2}\left(\frac{\partial^2 V}{\partial X^2}+\frac{\partial^2 V}{\partial Y^2}\right)+\frac{\kappa}{\rho u_o L}\frac{\partial W}{\partial X}+\frac{g\beta(\Theta_h-\Theta_c)L}{u_0^2}\theta,$$

$$\frac{\partial V}{\partial T}+U\frac{\partial V}{\partial X}+V\frac{\partial V}{\partial Y}+=-\frac{\partial P}{\partial Y}+\frac{\mu}{L\rho u_o}\left(\frac{\partial^2 V}{\partial X^2}+\frac{\partial^2 V}{\partial Y^2}\right)-\frac{K\mu}{\rho u_o L}\frac{\partial W}{\partial X}+\frac{Ge}{Re^2}\theta,$$

$$\frac{\partial V}{\partial T}+U\frac{\partial V}{\partial X}+V\frac{\partial V}{\partial Y}=-\frac{\partial P}{\partial Y}+\frac{1}{\frac{\rho L u_o}{\mu}}\left(\frac{\partial^2 V}{\partial X^2}+\frac{\partial^2 V}{\partial Y^2}\right)-\frac{K}{\frac{\rho L u_o}{\mu}}\frac{\partial W}{\partial X}+\frac{Ge}{Re^2}\theta,$$

$$\frac{\partial V}{\partial T}+U\frac{\partial V}{\partial X}+V\frac{\partial V}{\partial Y}=-\frac{\partial P}{\partial Y}+\frac{1}{Re}\left(\frac{\partial^2 V}{\partial X^2}+\frac{\partial^2 V}{\partial Y^2}\right)-\frac{K}{Re}\frac{\partial W}{\partial X}+\frac{Ge}{Re^2}\theta. \quad (3.8)$$

Now, the dimensionless form of the micro-rotational equation (3.4) can be obtained as follow:

$$\frac{\partial \omega}{\partial t}+u\frac{\partial \omega}{\partial x}+v\frac{\partial \omega}{\partial y}=\frac{\gamma}{\rho j}\left(\frac{\partial^2 \omega}{\partial x^2}+\frac{\partial^2 \omega}{\partial y^2}\right)+\frac{2\kappa}{\rho j}\left(\frac{\partial v}{\partial x}-\frac{\partial u}{\partial y}-2\omega\right),$$

$$\frac{u_o^2}{L^2}\frac{\partial W}{\partial T}+\frac{u_o^2}{L^2}U\frac{\partial W}{\partial X}+\frac{u_o^2}{L^2}V\frac{\partial W}{\partial Y}$$
$$\Rightarrow \frac{\gamma}{\rho j}\left(\frac{u_o}{L^3}\frac{\partial^2 W}{\partial X^2}+\frac{u_o}{L^3}\frac{\partial^2 W}{\partial Y^2}\right)+\frac{2\kappa u_0}{\rho j L}\left(\frac{\partial V}{\partial X}-\frac{\partial U}{\partial Y}-2W\right),$$

$$\frac{u_o^2}{L^2}\left[\frac{\partial W}{\partial T}+U\frac{\partial W}{\partial X}+V\frac{\partial W}{\partial Y}\right]$$
$$\Rightarrow \frac{u_o\gamma}{\rho j L^3}\left(\frac{\partial^2 W}{\partial X^2}+\frac{\partial^2 W}{\partial Y^2}\right)+\frac{2\kappa u_0}{\rho j L}\left(\frac{\partial V}{\partial X}-\frac{\partial U}{\partial Y}-2W\right),$$

$$\frac{\partial W}{\partial T}+U\frac{\partial W}{\partial X}+V\frac{\partial W}{\partial Y}=\frac{\mu}{L\rho u_0}\left(1+\frac{K}{2}\right)\left(\frac{\partial^2 W}{\partial X^2}+\frac{\partial^2 W}{\partial Y^2}\right)+\frac{2\kappa L}{\rho j u_0}\left(\frac{\partial V}{\partial X}-\frac{\partial U}{\partial Y}-2W\right),$$

$$\frac{\partial W}{\partial T}+U\frac{\partial W}{\partial X}+V\frac{\partial W}{\partial Y}=\frac{1}{\frac{L\rho u_0}{\mu}}\left(1+\frac{K}{2}\right)\left(\frac{\partial^2 W}{\partial X^2}+\frac{\partial^2 W}{\partial Y^2}\right)+\frac{2K\mu L^2}{\rho L j u_0}\left(\frac{\partial V}{\partial X}-\frac{\partial U}{\partial Y}-2W\right),$$

$$\frac{\partial W}{\partial T}+U\frac{\partial W}{\partial X}+V\frac{\partial W}{\partial Y}=\frac{1}{Re}\left(1+\frac{K}{2}\right)\left(\frac{\partial^2 W}{\partial X^2}+\frac{\partial^2 W}{\partial Y^2}\right)+\frac{2K}{\frac{j}{L^2}\frac{\rho L u_0}{\mu}}\left(\frac{\partial V}{\partial X}-\frac{\partial U}{\partial Y}-2W\right),$$

$$\frac{\partial W}{\partial T}+U\frac{\partial W}{\partial X}+V\frac{\partial W}{\partial Y}=\frac{1}{Re}\left(1+\frac{K}{2}\right)\left(\frac{\partial^2 W}{\partial X^2}+\frac{\partial^2 W}{\partial Y^2}\right)+\frac{2K}{E_r Re}\left(\frac{\partial V}{\partial X}-\frac{\partial U}{\partial Y}-2W\right). \tag{3.9}$$

Now, the non dimensional form of energy equation (3.5) can be obtained as:

$$\frac{\partial \Theta}{\partial t}+u\frac{\partial \Theta}{\partial x}+v\frac{\partial \Theta}{\partial y}=\alpha\left(\frac{\partial^2 \Theta}{\partial x^2}+\frac{\partial^2 \Theta}{\partial y^2}\right),$$

$$(\Theta_h-\Theta_c)\frac{u_o}{L}\frac{\partial \theta}{\partial T}+(\Theta_h-\Theta_c)U\frac{u_o}{L}\frac{\partial \theta}{\partial X}+(\Theta_h-\Theta_c)V\frac{u_o}{L}\frac{\partial \theta}{\partial Y}$$
$$\Rightarrow \frac{\alpha(\Theta_h-\Theta_c)}{L^2}\frac{\partial^2 \theta}{\partial X^2}+\frac{\alpha(\Theta_h-\Theta_c)}{L^2}\frac{\partial^2 \theta}{\partial Y^2},$$

$$(\Theta_h-\Theta_c)\frac{u_o}{L}\left(\frac{\partial \theta}{\partial T}+U\frac{\partial \theta}{\partial X}+V\frac{\partial \theta}{\partial Y}\right)=\frac{\alpha(\Theta_h-\Theta_c)}{L^2}\left(\frac{\partial^2 \theta}{\partial X^2}+\frac{\partial^2 \theta}{\partial Y^2}\right),$$
$$\left(\frac{\partial \theta}{\partial T}+U\frac{\partial \theta}{\partial X}+V\frac{\partial \theta}{\partial Y}\right)=\frac{\alpha}{u_0 L}\left(\frac{\partial^2 \theta}{\partial X^2}+\frac{\partial^2 \theta}{\partial Y^2}\right),$$
$$\left(\frac{\partial \theta}{\partial T}+U\frac{\partial \theta}{\partial X}+V\frac{\partial \theta}{\partial Y}\right)=\frac{k_t}{\rho c_p}\frac{1}{L u_0}\left(\frac{\partial^2 \theta}{\partial X^2}+\frac{\partial^2 \theta}{\partial Y^2}\right),$$
$$\left(\frac{\partial \theta}{\partial T}+U\frac{\partial \theta}{\partial X}+V\frac{\partial \theta}{\partial Y}\right)=\frac{k_t}{\mu c_p}\frac{\mu}{\rho L u_0}\left(\frac{\partial^2 \theta}{\partial X^2}+\frac{\partial^2 \theta}{\partial Y^2}\right),$$
$$\left(\frac{\partial \theta}{\partial T}+U\frac{\partial \theta}{\partial X}+V\frac{\partial \theta}{\partial Y}\right)=\frac{1}{PrRe}\left(\frac{\partial^2 \theta}{\partial X^2}+\frac{\partial^2 \theta}{\partial Y^2}\right). \tag{3.10}$$

Dimensionless Governing Equations:These transformations leads to the following system of governing equations:

i. Continuity equation

$$\frac{\partial U}{\partial X}+\frac{\partial V}{\partial Y}=0. \tag{3.11}$$

ii. Momentum equation for U-velocity

$$\frac{\partial U}{\partial T}+U\frac{\partial U}{\partial X}+V\frac{\partial U}{\partial Y}=-\frac{\partial P}{\partial X}+\frac{1}{Re}\left(\frac{\partial^2 U}{\partial X^2}+\frac{\partial^2 U}{\partial Y^2}\right)+\frac{K}{Re}\frac{\partial W}{\partial Y}. \tag{3.12}$$

iii. Momentum equation for V velocity

$$\frac{\partial V}{\partial T}+U\frac{\partial V}{\partial X}+V\frac{\partial V}{\partial Y}=-\frac{\partial P}{\partial Y}+\frac{1}{Re}\left(\frac{\partial^2 V}{\partial X^2}+\frac{\partial^2 V}{\partial Y^2}\right)-\frac{K}{Re}\frac{\partial W}{\partial X}+\frac{Gr}{Re^2}\theta. \tag{3.13}$$

iv. Microrotational equation

$$\begin{aligned}&\frac{\partial W}{\partial T}+U\frac{\partial W}{\partial X}+V\frac{\partial W}{\partial Y}\\&=\frac{1}{Re}\left(1+\frac{K}{2}\right)\left(\frac{\partial^2 W}{\partial X^2}+\frac{\partial^2 W}{\partial Y^2}\right)+\frac{2K}{E_R Re}\left(\frac{\partial V}{\partial X}-\frac{\partial U}{\partial Y}-2W\right).\end{aligned} \tag{3.14}$$

v. Energy equation

$$\frac{\partial \theta}{\partial T}+U\frac{\partial \theta}{\partial X}+V\frac{\partial \theta}{\partial Y}=\frac{1}{RePr}\left(\frac{\partial^2 \theta}{\partial X^2}+\frac{\partial^2 \theta}{\partial Y^2}\right). \tag{3.15}$$

The above system of equations are subject to following boundary conditions:

At Left:

$$on\ \ L1: \quad U=1, \quad V=0, \quad W=0,$$

$$on\ \ L2: \quad U=0, \quad V=0, \quad W=0,$$

$$on\ \ L3: \quad U=0, \quad V=0, \quad W=0, \quad \theta=1.$$

At Right:

$$on\ \ R1: \quad \frac{\partial U}{\partial X}=0, \quad \frac{\partial V}{\partial X}=0, \quad \frac{\partial W}{\partial X}=0, \quad \frac{\partial \theta}{\partial X}=0.$$

$$on\ \ R2: \quad U=0, \quad V=0, \quad W=0, \quad \frac{\partial \theta}{\partial X}=0,$$

$$on\ \ R3: \quad U=0, \quad V=0, \quad W=0,$$

At Top:

$$U = 0, \quad V = 0, \quad W = 0, \quad \frac{\partial \theta}{\partial Y} = 0,$$

At Bottom:

$$U = 0, \quad V = 0, \quad W = 0, \quad \frac{\partial \theta}{\partial Y} = 0,$$

In Eq.3.12- Eq.3.15, the non-dimensional parameters Re represent Reynolds number, K is Micro-polar flow, Pr represents Prandtl number, Gr is the Grashof number, Er is Eringen parameter, respectively defined by

$$\begin{aligned} Re &= \frac{\rho L U_o}{\mu}, \quad & K &= \frac{k}{\mu}, \quad & E_r &= \frac{j}{L^2}, \\ Pr &= \frac{\mu c_p}{k_t}, \quad & Gr &= \frac{g\beta(\Theta_h - \Theta_c)L^3}{v^2}. \end{aligned} \tag{3.16}$$

3.3 Numerical Procedure of Galerkin Based Finite Element Formation

The Non linear Partial Differential Equations with associated boundary conditions are solved using Galerkin based Finite Element Method.

First, the weak formulation of the governing equations is derived and then the solution is approximated by using the Galerkin approximation method.

3.3.1 Variational Formation

The goal of variational formulation is to convert the governing equations into integral equations. By multiplying PDEs by test functions in the same space, the equations are converted from the strong form to the weak form after being integrated over the entire domain.

Finally, we were able to obtain an approximate solution by choosing the set of approximate trial functions valid only on a part of the domain.

Weak Formulation: The weak form of continuity equation (3.11) are as follow:

$$\frac{\partial U}{\partial X} + \frac{\partial V}{\partial Y} = 0,$$

Multiplying by test function ϕ and integrate over computational domain,

$$\int_{\Omega} \Phi(\frac{\partial U}{\partial X} + \frac{\partial V}{\partial Y}) d\Omega = 0. \tag{3.17}$$

.

The weak form for U-component Eq.3.12 are as follow

$$\frac{\partial U}{\partial T} + U\frac{\partial U}{\partial X} + V\frac{\partial U}{\partial Y} = -\frac{\partial P}{\partial X} + \frac{1}{Re}\left(\frac{\partial^2 U}{\partial X^2} + \frac{\partial^2 U}{\partial Y^2}\right) + \frac{K}{Re}\frac{\partial W}{\partial Y}.$$

Multiplying by test function Φ_1 first

$$\Phi_1(\frac{\partial U}{\partial T}) + \Phi_1\left[\left(U\frac{\partial U}{\partial X}\right) + \left(V\frac{\partial U}{\partial Y}\right)\right] = -\Phi_1\frac{\partial P}{\partial X} + \frac{1}{Re}\Phi_1\left\{\frac{\partial^2 U}{\partial X^2} + \frac{\partial^2 U}{\partial Y^2}\right\} + \frac{K}{Re}\Phi_1\frac{\partial W}{\partial Y},$$

and integrate over computational domain Ω, implies

$$\int_{\Omega} \Phi_1(\frac{\partial U}{\partial T}) d\Omega + \int_{\Omega} \Phi_1\left[\left(U\frac{\partial U}{\partial X}\right) + \left(V\frac{\partial U}{\partial Y}\right)\right] d\Omega = -\int_{\Omega} \Phi_1\frac{\partial P}{\partial X} d\Omega + \frac{1}{Re}\int_{\Omega} \Phi_1\left\{\frac{\partial^2 U}{\partial X^2} + \frac{\partial^2 U}{\partial Y^2}\right\} d\Omega + \frac{K}{Re}\int_{\Omega} \Phi_1\frac{\partial W}{\partial Y} d\Omega,$$

$$\Rightarrow \int_{\Omega} \Phi_1(\frac{\partial U}{\partial T}) d\Omega + \int_{\Omega} \Phi_1\left[\left(U\frac{\partial U}{\partial X}\right) + \left(V\frac{\partial U}{\partial Y}\right)\right] d\Omega = -\int_{\Omega} \Phi_1\frac{\partial P}{\partial X} d\Omega + \frac{1}{Re}\int_{\Omega} \Phi_1\left\{(\nabla^2 U)\right\} d\Omega + \frac{K}{Re}\int_{\Omega} \Phi_1\frac{\partial W}{\partial Y} d\Omega.$$

Now, applying Green's theorem to the diffusion term,

$$\int_{\Omega} \Phi_1(\nabla^2 U) d\Omega = -\int_{\Omega} (\nabla\Phi_1.\nabla U) d\Omega + \int_{\Gamma} \Phi_1(\frac{\partial U}{\partial n}) d\Gamma,$$

Substituting,

$$\frac{1}{Re}\int_{\Omega} \Phi_1(\nabla^2 U) d\Omega = -\frac{1}{Re}\int_{\Omega} (\nabla\Phi_1.\nabla U) d\Omega + \frac{1}{Re}\int_{\Gamma} \Phi_1(\frac{\partial U}{\partial n}) d\Gamma.$$

Now, applying by part integration to the pressure term,

$$\int_\Omega \Phi_1 \frac{\partial P}{\partial X} d\Omega = -\int_\Omega P \frac{\partial \Phi_1}{\partial X} d\Omega + \int_\Gamma \Phi_1 P n_x d\Gamma,$$
$$\Rightarrow -\int_\Omega \Phi_1 \frac{\partial P}{\partial X} d\Omega = \int_\Omega P \frac{\partial \Phi_1}{\partial X} d\Omega - \int_\Gamma \Phi_1 P n_x d\Gamma.$$

Substituting, the diffusion and pressure terms into the integral equation gives,

$$\begin{aligned}
&\int_\Omega \Phi_1 (\frac{\partial U}{\partial T}) d\Omega + \int_\Omega \Phi_1 \left[\left(U \frac{\partial U}{\partial X} \right) + \left(V \frac{\partial U}{\partial Y} \right) \right] d\Omega = \int_\Omega P \frac{\partial \Phi_1}{\partial X} d\Omega - \int_\Gamma \Phi_1 P n_x d\Gamma \\
&\qquad - \frac{1}{Re} \int_\Omega (\nabla \Phi_1 . \nabla U) d\Omega + \frac{1}{Re} \int_\Gamma \Phi_1 (\frac{\partial U}{\partial n}) d\Gamma + \frac{K}{Re} \int_\Omega \Phi_1 \frac{\partial W}{\partial Y} d\Omega, \\
\Rightarrow &\int_\Omega \Phi_1 (\frac{\partial U}{\partial T}) d\Omega + \int_\Omega \Phi_1 \left[\left(U \frac{\partial U}{\partial X} \right) + \left(V \frac{\partial U}{\partial Y} \right) \right] d\Omega - \int_\Omega P \frac{\partial \Phi_1}{\partial X} d\Omega \\
&+ \frac{1}{Re} \int_\Omega (\nabla \Phi_1 . \nabla U) d\Omega - \frac{K}{Re} \int_\Omega \Phi_1 \frac{\partial W}{\partial Y} d\Omega = -\int_\Gamma \Phi_1 P n_x d\Gamma + \frac{1}{Re} \int_\Gamma \Phi_1 (\frac{\partial U}{\partial n}) d\Gamma.
\end{aligned} \tag{3.18}$$

which is the required weak form of U-momentum.

The weak form for V-momentum Eq.3.13 are as follow:

$$\frac{\partial V}{\partial T} + U \frac{\partial V}{\partial X} + V \frac{\partial V}{\partial Y} = -\frac{\partial P}{\partial Y} + \frac{1}{Re} \left(\frac{\partial^2 V}{\partial X^2} + \frac{\partial^2 V}{\partial Y^2} \right) - \frac{K}{Re} \frac{\partial W}{\partial X} + \frac{Gr}{Re^2} \theta$$

Multiplying by test function Φ_2 first

$$\begin{aligned}
&\Phi_2 \frac{\partial V}{\partial T} + \Phi_2 \left(U \frac{\partial V}{\partial X} + V \frac{\partial V}{\partial Y} \right) \\
&\qquad = -\Phi_2 \frac{\partial P}{\partial Y} + \Phi_2 \frac{1}{Re} \left(\frac{\partial^2 V}{\partial X^2} + \frac{\partial^2 V}{\partial Y^2} \right) - \Phi_2 \frac{K}{Re} \frac{\partial W}{\partial X} + \Phi_2 \frac{Gr}{Re^2} \theta,
\end{aligned}$$

and integrate over computational domain Ω, implies

$$\begin{aligned}
&\int_\Omega \Phi_2 (\frac{\partial V}{\partial T}) d\Omega + \int_\Omega \Phi_2 \left[\left(U \frac{\partial V}{\partial X} \right) + \left(V \frac{\partial V}{\partial Y} \right) \right] d\Omega \\
&= -\int_\Omega \Phi_2 \frac{\partial P}{\partial Y} d\Omega + \frac{1}{Re} \int_\Omega \Phi_2 \left\{ \frac{\partial^2 V}{\partial X^2} + \frac{\partial^2 V}{\partial Y^2} \right\} d\Omega - \frac{K}{Re} \int_\Omega \Phi_2 \frac{\partial W}{\partial X} d\Omega + \\
&\qquad \frac{Gr}{Re^2} \int_\Omega \Phi_2 \theta d\Omega,
\end{aligned}$$

$$\int_\Omega \Phi_2(\frac{\partial V}{\partial T})d\Omega + \int_\Omega \Phi_2\left[\left(U\frac{\partial V}{\partial X}\right) + \left(V\frac{\partial V}{\partial Y}\right)\right]d\Omega$$
$$= -\int_\Omega \Phi_2\frac{\partial P}{\partial Y}d\Omega + \frac{1}{Re}\int_\Omega \Phi_2\left\{(\nabla^2 V)\right\}d\Omega - \frac{K}{Re}\int_\Omega \Phi_2\frac{\partial W}{\partial X}d\Omega + \frac{Gr}{Re^2}\int_\Omega \Phi_2\theta d\Omega.$$

Now, applying Green's theorem to the diffusion term,

$$\int_\Omega \Phi_2(\nabla^2 V)d\Omega = -\int_\Omega (\nabla\Phi_2.\nabla V)d\Omega + \int_\Gamma \Phi_2(\frac{\partial V}{\partial n})d\Gamma,$$

Since,

$$\frac{1}{Re}\int_\Omega \Phi_2(\nabla^2 V)d\Omega = -\frac{1}{Re}\int_\Omega (\nabla\Phi_2.\nabla V)d\Omega + \frac{1}{Re}\int_\Gamma \Phi_2(\frac{\partial V}{\partial n})d\Gamma.$$

Now, applying by part integration to the pressure term,

$$\int_\Omega \Phi_2\frac{\partial P}{\partial Y}d\Omega = -\int_\Omega P\frac{\partial \Phi_2}{\partial Y}d\Omega + \int_\Gamma \Phi_2 P n_y d\Gamma,$$

$$\Rightarrow -\int_\Omega \Phi_2\frac{\partial P}{\partial Y}d\Omega = \int_\Omega P\frac{\partial \Phi_2}{\partial Y}d\Omega - \int_\Gamma \Phi_2 P n_y d\Gamma.$$

Substituting, the diffusion and pressure terms into the integral equation gives,

$$\int_\Omega \Phi_2(\frac{\partial V}{\partial T})d\Omega + \int_\Omega \Phi_2\left[\left(U\frac{\partial V}{\partial X}\right) + \left(V\frac{\partial V}{\partial Y}\right)\right]d\Omega = \int_\Omega P\frac{\partial \Phi_2}{\partial Y}d\Omega - \int_\Gamma \Phi_2 P n_y d\Gamma$$
$$-\frac{1}{Re}\int_\Omega (\nabla\Phi_2.\nabla V)d\Omega + \frac{1}{Re}\int_\Gamma \Phi_2(\frac{\partial V}{\partial n})d\Gamma - \frac{K}{Re}\int_\Omega \Phi_2\frac{\partial W}{\partial X}d\Omega +$$
$$\frac{Gr}{Re^2}\int_\Omega \Phi_2\theta d\Omega,$$

$$\Rightarrow \int_\Omega \Phi_2(\frac{\partial V}{\partial T})d\Omega + \int_\Omega \Phi_2\left[\left(U\frac{\partial V}{\partial X}\right) + \left(V\frac{\partial V}{\partial Y}\right)\right]d\Omega - \int_\Omega P\frac{\partial \Phi_2}{\partial Y}d\Omega +$$
$$\frac{1}{Re}\int_\Omega (\nabla\Phi_2.\nabla V)d\Omega + \frac{K}{Re}\int_\Omega \Phi_2\frac{\partial W}{\partial X}d\Omega - \frac{Gr}{Re^2}\int_\Omega \Phi_2\theta d\Omega \qquad (3.19)$$
$$= -\int_\Gamma \Phi_2 P n_y d\Gamma + \frac{1}{Re}\int_\Gamma \Phi_2(\frac{\partial V}{\partial n})d\Gamma.$$

which is the required weak form of V-momentum. The weak form for microrotational equation (3.14) are as follow:

$$\frac{\partial W}{\partial T} + U\frac{\partial W}{\partial X} + V\frac{\partial W}{\partial Y} = \frac{1}{Re}\left(1+\frac{K}{2}\right)\left(\frac{\partial^2 W}{\partial X^2} + \frac{\partial^2 W}{\partial Y^2}\right) + \frac{2K}{E_R Re}\left(\frac{\partial V}{\partial X} - \frac{\partial U}{\partial Y} - 2W\right).$$

Multiplying by test function Ψ first,

$$\Psi\frac{\partial W}{\partial T}+\Psi\left(U\frac{\partial W}{\partial X}+V\frac{\partial W}{\partial Y}\right)=\frac{1}{Re}\left(1+\frac{K}{2}\right)\Psi\left(\frac{\partial^2 W}{\partial X^2}+\frac{\partial^2 W}{\partial Y^2}\right)+\frac{2K}{E_R Re}\Psi\left(\frac{\partial V}{\partial X}-\frac{\partial U}{\partial Y}-2W\right),$$

Integrate over computational domain Ω, implies

$$\int_\Omega \Psi\frac{\partial W}{\partial T}d\Omega+\int_\Omega \Psi\left(U\frac{\partial W}{\partial X}+V\frac{\partial W}{\partial Y}\right)d\Omega = \frac{1}{Re}\left(1+\frac{K}{2}\right)\int_\Omega \Psi\left(\frac{\partial^2 W}{\partial X^2}+\frac{\partial^2 W}{\partial Y^2}\right)d\Omega$$

$$+\frac{2K}{E_R Re}\int_\Omega \Psi\left(\frac{\partial V}{\partial X}-\frac{\partial U}{\partial Y}-2W\right)d\Omega,$$

$$\Rightarrow \int_\Omega \Psi\frac{\partial W}{\partial T}d\Omega+\int_\Omega \Psi\left(U\frac{\partial W}{\partial X}+V\frac{\partial W}{\partial Y}\right)d\Omega=\frac{1}{Re}\left(1+\frac{K}{2}\right)\int_\Omega \Psi\nabla^2 W d\Omega$$

$$+\frac{2K}{E_R Re}\int_\Omega \Psi\left(\frac{\partial V}{\partial X}-\frac{\partial U}{\partial Y}-2W\right)d\Omega,$$

Now, applying Green's theorem to the diffusion term,

$$\int_\Omega \Psi(\nabla^2 W)d\Omega=-\int_\Omega(\nabla\Psi.\nabla W)d\Omega+\int_\Gamma \Psi(\frac{\partial W}{\partial n})d\Gamma,$$

since,

$$\frac{1}{Re}\left(1+\frac{K}{2}\right)\int_\Omega \Psi(\nabla^2 W)d\Omega=-\frac{1}{Re}\left(1+\frac{K}{2}\right)\int_\Omega(\nabla\Psi.\nabla W)d\Omega+\frac{1}{Re}\left(1+\frac{K}{2}\right)\int_\Gamma \Psi(\frac{\partial W}{\partial n})d\Gamma.$$

Substituting the diffusion term into the integral term gives,

$$\int_\Omega \Psi\frac{\partial W}{\partial T}d\Omega+\int_\Omega \Psi\left(U\frac{\partial W}{\partial X}+V\frac{\partial W}{\partial Y}\right)d\Omega=-\frac{1}{Re}\left(1+\frac{K}{2}\right)\int_\Omega(\nabla\Psi.\nabla W)d\Omega$$

$$+\frac{1}{Re}\left(1+\frac{K}{2}\right)\int_\Gamma \Psi(\frac{\partial W}{\partial n})d\Gamma+\frac{2K}{E_R Re}\int_\Omega \Psi\left(\frac{\partial V}{\partial X}-\frac{\partial U}{\partial Y}-2W\right)d\Omega,$$

$$\Rightarrow \int_\Omega \Psi \frac{\partial W}{\partial T} d\Omega + \int_\Omega \Psi \left(U\frac{\partial W}{\partial X} + V\frac{\partial W}{\partial Y} \right) d\Omega + \frac{1}{Re}\left(1+\frac{K}{2}\right)\int_\Omega (\nabla\Psi.\nabla W) d\Omega$$
$$- \frac{2K}{E_R Re}\int_\Omega \Psi \left(\frac{\partial V}{\partial X} - \frac{\partial U}{\partial Y} - 2W \right) d\Omega = \frac{1}{Re}\left(1+\frac{K}{2}\right)\int_\Gamma \Psi(\frac{\partial W}{\partial n}) d\Gamma. \tag{3.20}$$

which is required weak form of microrotational equation.

The weak form for energy equation (3.15) are as follow:

$$\frac{\partial \theta}{\partial T} + U\frac{\partial \theta}{\partial X} + V\frac{\partial \theta}{\partial Y} = \frac{1}{RePr}\left(\frac{\partial^2 \theta}{\partial X^2} + \frac{\partial^2 \theta}{\partial Y^2} \right),$$

Multiplying by test function η first,

$$\eta\frac{\partial \theta}{\partial T} + \eta\left(U\frac{\partial \theta}{\partial X} + V\frac{\partial \theta}{\partial Y} \right) = \frac{1}{RePr}\eta\left(\frac{\partial^2 \theta}{\partial X^2} + \frac{\partial^2 \theta}{\partial Y^2} \right),$$

Integrate over computational domain Ω

, gives

$$\int_\Omega \eta\frac{\partial \theta}{\partial T} d\Omega + \int_\Omega \eta\left(U\frac{\partial \theta}{\partial X} + V\frac{\partial \theta}{\partial Y} \right) d\Omega = \frac{1}{RePr}\int_\Omega \eta\left(\frac{\partial^2 \theta}{\partial X^2} + \frac{\partial^2 \theta}{\partial Y^2} \right) d\Omega,$$

$$\Rightarrow \int_\Omega \eta\frac{\partial \theta}{\partial T} d\Omega + \int_\Omega \eta\left(U\frac{\partial \theta}{\partial X} + V\frac{\partial \theta}{\partial Y} \right) d\Omega = \frac{1}{RePr}\int_\Omega \eta\nabla^2\theta d\Omega.$$

Now, applying Green's theorem to the diffusion term,

$$\int_\Omega \eta(\nabla^2\theta) d\Omega = -\int_\Omega (\nabla\eta.\nabla\theta) d\Omega + \int_\Gamma \eta(\frac{\partial \theta}{\partial n}) d\Gamma,$$

since,

$$\frac{1}{RePr}\int_\Omega \eta(\nabla^2\theta) d\Omega = -\frac{1}{RePr}\int_\Omega (\nabla\eta.\nabla\theta) d\Omega + \frac{1}{RePr}\int_\Gamma \eta(\frac{\partial \theta}{\partial n}) d\Gamma,$$

Substituting the diffusion term into the integral term gives,

$$\int_\Omega \eta\frac{\partial \theta}{\partial T} d\Omega + \int_\Omega \eta\left(U\frac{\partial \theta}{\partial X} + V\frac{\partial \theta}{\partial Y} \right) d\Omega = -\frac{1}{RePr}\int_\Omega (\nabla\eta.\nabla\theta) d\Omega + \frac{1}{RePr}\int_\Gamma \eta(\frac{\partial \theta}{\partial n}) d\Gamma,$$

$$\Rightarrow \int_\Omega \eta \frac{\partial \theta}{\partial T}\, d\Omega + \int_\Omega \eta \left(U \frac{\partial \theta}{\partial X} + V \frac{\partial \theta}{\partial Y} \right) d\Omega + \frac{1}{Re\, Pr} \int_\Omega (\nabla \eta \cdot \nabla \theta)\, d\Omega = \frac{1}{Re\, Pr} \int_\Gamma \eta \left(\frac{\partial \theta}{\partial n} \right) d\Gamma. \tag{3.21}$$

which is the required weak form of energy equation.

3.3.2 Finite Element Approximation

The variational forms of the governing equations are obtained and then the problem is discretized using the Galerkin finite element method. Let N_i denote shape functions of finite elements that correspond to the nodes of the elements. The dependent variables are assumed to be approximately:

$$U_h = \sum_{j=1}^{n} U_j N_j, \qquad V_h = \sum_{j=1}^{n} V_j N_j, \qquad W_h = \sum_{j=1}^{n} W_j N_j,$$
$$P_h = \sum_{j=1}^{n} P_j N_j, \qquad \theta_h = \sum_{j=1}^{n} \theta_j N_j.$$

where, $U_j, V_j, P_j, W_j, \Theta_j$ are the nodal values of the variables while $n =$ is the number of nodes per element.

Now, the Galerkin approach uses weight functions (test functions) that belongs to same approximation space as test function:

$\Phi_1 = N_i, \qquad \Phi_2 = N_i, \qquad \Psi = N_i, \qquad \eta = N_i, \qquad \Phi = N_i.$

The finite element equations obtained by substituting these finite element into the weak formulations, are the discrete finite element equations.

Substituting,the finite element approximations into the weak form of continuity equation (3.17),

$$\int_\Omega N_i \left(\frac{\partial \sum_{j=1}^{n} U_j N_j}{\partial X} + \frac{\partial \sum_{j=1}^{n} V_j N_j}{\partial Y} \right) d\Omega = 0,$$

$$\Rightarrow \sum_{j=1}^{n} \left(\int_\Omega N_i \left(\frac{\partial N_j}{\partial X} d\Omega \right) U_j + \sum_{j=1}^{n} \left(\int_\Omega N_i \left(\frac{\partial N_j}{\partial Y} d\Omega \right) V_j = 0. \right. \right.$$

Defining, $(D_x)_{ij} = \int_\Omega N_i \frac{\partial N_j}{\partial X} d\Omega$ and $(D_y)_{ij} = \int_\Omega N_i \frac{\partial N_j}{\partial Y} d\Omega$.
Therefore, it yields the discrete incompressibility constraint,

$$D_x U + D_y V = 0. \tag{3.22}$$

Now substituting the finite element approximations into the weak form of U-momentum equation (3.18) gives,

$$\int_\Omega N_i \left(\frac{\partial \left(\sum_{j=1}^n U_j N_j \right)}{\partial T} \right) d\Omega + \int_\Omega N_i \Bigg[\left(\sum_{j=1}^n U_j N_j \right) \frac{\partial \left(\sum_{k=1}^n U_k N_k \right)}{\partial X} + \left(\sum_{j=1}^n V_j N_j \right) \frac{\partial \left(\sum_{k=1}^n U_k N_k \right)}{\partial Y} \Bigg] d\Omega - \int_\Omega \left(\sum_{j=1}^n P_j N_j \right) \frac{\partial N_i}{\partial X} \, d\Omega + \frac{1}{Re} \int_\Omega \left(\nabla N_i \cdot \nabla \sum_{j=1}^n U_j N_j \right) d\Omega - \frac{K}{Re} \int_\Omega N_i \frac{\partial \left(\sum_{j=1}^n W_j N_j \right)}{\partial Y} \, d\Omega = F_u.$$

$$\Rightarrow \sum_{j=1}^n \left(\int_\Omega N_i N_j \, d\Omega \right) \frac{\partial U_j}{\partial T} + \int_\Omega N_i \Bigg[\left(\sum_{j=1}^n U_j N_j \right) \left(\sum_{k=1}^n \frac{\partial N_k}{\partial X} U_k \right) + \left(\sum_{j=1}^n V_j N_j \right) \left(\sum_{k=1}^n \frac{\partial N_k}{\partial Y} U_k \right) \Bigg] d\Omega - \sum_{j=1}^n \left(\int_\Omega N_j \frac{\partial N_i}{\partial X} \, d\Omega \right) P_j + \frac{1}{Re} \sum_{j=1}^n \left(\int_\Omega \nabla N_i \cdot \nabla N_j \, d\Omega \right) U_j - \frac{K}{Re} \sum_{j=1}^n \left(\int_\Omega N_i \frac{\partial N_j}{\partial Y} \, d\Omega \right) W_j = F_u.$$

Defining,

$$M_{ij} = \int_\Omega N_i N_j d\Omega), \qquad K_{ij} = \int_\Omega (\nabla N_i . \nabla N_j) d\Omega, \qquad (G_x)_{ij} = \int_\Omega N_j \frac{\partial N_i}{\partial X} d\Omega$$
$$(C_y)_{ij} = \int_\Omega N_i \frac{\partial N_j}{\partial Y} d\Omega,$$

Here, The non linear convective contribution is linearized and denoted compactly by the convection matrix $N(U)$. So, the element equation for U-momentum can be written as,

$$M\frac{\partial U}{\partial T} + N(U)U - G_x P + \frac{1}{Re}KU - \frac{K}{Re}C_y W = F_u. \tag{3.23}$$

Now substituting the finite element approximations into the weak form of V-momentum equation (3.19) gives,

$$\begin{aligned}
&\int_\Omega N_i \left(\frac{\partial \left(\sum_{j=1}^{n} V_j N_j \right)}{\partial T} \right) d\Omega + \int_\Omega N_i \left[\left(\sum_{j=1}^{n} U_j N_j \right) \frac{\partial \left(\sum_{k=1}^{n} V_k N_k \right)}{\partial X} \right. \\
&\left. + \left(\sum_{j=1}^{n} V_j N_j \right) \frac{\partial \left(\sum_{k=1}^{n} V_k N_k \right)}{\partial Y} \right] d\Omega - \int_\Omega \left(\sum_{j=1}^{n} P_j N_j \right) \frac{\partial N_i}{\partial Y}\, d\Omega \\
&+ \frac{1}{Re} \int_\Omega \left(\nabla N_i \cdot \nabla \sum_{j=1}^{n} V_j N_j \right) d\Omega + \frac{K}{Re} \int_\Omega N_i \frac{\partial \left(\sum_{j=1}^{n} W_j N_j \right)}{\partial X}\, d\Omega \\
&- \frac{Gr}{Re^2} \int_\Omega N_i \left(\sum_{j=1}^{n} \theta_j N_j \right) d\Omega = F_v.
\end{aligned}$$

$$\begin{aligned}
\Rightarrow &\sum_{j=1}^{n} \left(\int_\Omega N_i N_j\, d\Omega \right) \frac{\partial V_j}{\partial T} + \int_\Omega N_i \left[\left(\sum_{j=1}^{n} U_j N_j \right) \left(\sum_{k=1}^{n} \frac{\partial N_k}{\partial X} V_k \right) \right. \\
&\left. + \left(\sum_{j=1}^{n} V_j N_j \right) \left(\sum_{k=1}^{n} \frac{\partial N_k}{\partial Y} V_k \right) \right] d\Omega - \sum_{j=1}^{n} \left(\int_\Omega N_j \frac{\partial N_i}{\partial Y}\, d\Omega \right) P_j \\
&+ \frac{1}{Re} \sum_{j=1}^{n} \left(\int_\Omega \nabla N_i \cdot \nabla N_j\, d\Omega \right) V_j + \frac{K}{Re} \sum_{j=1}^{n} \left(\int_\Omega N_i \frac{\partial N_j}{\partial X}\, d\Omega \right) W_j \\
&- \frac{Gr}{Re^2} \sum_{j=1}^{n} \left(\int_\Omega N_i N_j\, d\Omega \right) \theta_j = F_v.
\end{aligned}$$

Defining,

$$M_{ij} = \int_\Omega N_i N_j d\Omega, \qquad K_{ij} = \int_\Omega (\nabla N_i . \nabla N_j) d\Omega, \qquad (G_y)_{ij} = \int_\Omega N_j \frac{\partial N_i}{\partial Y} d\Omega$$
$$(C_x)_{ij} = \int_\Omega N_i \frac{\partial N_j}{\partial X} d\Omega, \qquad B_{ij} = \frac{Gr}{Re^2} (\int_\Omega N_i N_j d\Omega),$$

Here, The non linear convective contribution is linearized and denoted compactly by the convection matrix $N(V)$. So, the element equation for V-momentum can be written as,

$$M\frac{\partial V}{\partial T} + N(V)V - G_y P + \frac{1}{Re} KV + \frac{K}{Re} C_x W - B\theta = F_v. \tag{3.24}$$

Now substituting the finite element approximations into the weak form of microrotational equation equation (3.20) gives,

$$\int_\Omega N_i \left(\frac{\partial \left(\sum_{j=1}^n W_j N_j \right)}{\partial T} \right) d\Omega + \int_\Omega N_i \Bigg[\left(\sum_{j=1}^n U_j N_j \right) \frac{\partial \left(\sum_{k=1}^n W_k N_k \right)}{\partial X}$$
$$+ \left(\sum_{j=1}^n V_j N_j \right) \frac{\partial \left(\sum_{k=1}^n W_k N_k \right)}{\partial Y} \Bigg] d\Omega$$
$$- + \frac{1}{Re} \left(1 + \frac{K}{2} \right) \int_\Omega \left(\nabla N_i \cdot \nabla \sum_{j=1}^n W_j N_j \right) d\Omega$$
$$- \frac{2K}{E_R \, Re} \int_\Omega N_i \left(\frac{\partial \left(\sum_{j=1}^n V_j N_j \right)}{\partial X} - \frac{\partial \left(\sum_{j=1}^n U_j N_j \right)}{\partial Y} - 2 \sum_{j=1}^n W_j N_j \right) d\Omega = F_w,$$

$$\Rightarrow \sum_{j=1}^n \left(\int_\Omega N_i N_j \, d\Omega \right) \frac{\partial W_j}{\partial T} + \int_\Omega N_i \Bigg[\left(\sum_{j=1}^n U_j N_j \right) \left(\sum_{k=1}^n \frac{\partial N_k}{\partial X} W_k \right)$$
$$+ \left(\sum_{j=1}^n V_j N_j \right) \left(\sum_{k=1}^n \frac{\partial N_k}{\partial Y} W_k \right) \Bigg] d\Omega + \frac{1}{Re} \left(1 + \frac{K}{2} \right) \sum_{j=1}^n \left(\int_\Omega \nabla N_i \cdot \nabla N_j \, d\Omega \right) W_j$$
$$- \frac{2K}{E_R \, Re} \int_\Omega N_i \left(\sum_{j=1}^n \frac{\partial N_j}{\partial X} V_j - \sum_{j=1}^n \frac{\partial N_j}{\partial Y} U_j - 2 \sum_{j=1}^n N_j W_j \right) d\Omega = F_w.$$

Defining,

$$M_{ij} = \int_\Omega N_i N_j d\Omega, \qquad K_{ij} = \int_\Omega (\nabla N_i . \nabla N_j) d\Omega, \qquad (C_{vx})_{ij} = \int_\Omega N_i \frac{\partial N_j}{\partial X} d\Omega$$
$$(C_{uy})_{ij} = \int_\Omega N_i \frac{\partial N_j}{\partial Y} d\Omega, \qquad S_{ij} = \int_\Omega N_i N_j d\Omega).$$

Here, The non linear convective contribution is linearized and denoted compactly by the convection matrix $N(W)$. So, the element equation for micro-rotational can be written as,

$$M\frac{\partial W}{\partial T} + N(W)W + \frac{1}{Re}\left(1 + \frac{K}{2}\right)KW - \frac{2K}{E_r Re}(C_{vx}V - C_{uy}U - 2SW) = F_w. \quad (3.25)$$

Now substituting the finite element approximations into the weak form of energy equation (3.21) gives,

$$\int_\Omega N_i \left(\frac{\partial\left(\sum_{j=1}^n \theta_j N_j\right)}{\partial T}\right) d\Omega + \int_\Omega N_i \left[\left(\sum_{j=1}^n U_j N_j\right) \frac{\partial\left(\sum_{k=1}^n \theta_k N_k\right)}{\partial X}\right.$$
$$\left. + \left(\sum_{j=1}^n V_j N_j\right) \frac{\partial\left(\sum_{k=1}^n \theta_k N_k\right)}{\partial Y}\right] d\Omega + \frac{1}{RePr}\int_\Omega \left(\nabla N_i \cdot \nabla \sum_{j=1}^n \theta_j N_j\right) d\Omega = F_\theta,$$

$$\Rightarrow \sum_{j=1}^n \left(\int_\Omega N_i N_j \, d\Omega\right) \frac{\partial \theta_j}{\partial T} + \int_\Omega N_i \left[\left(\sum_{j=1}^n U_j N_j\right)\left(\sum_{k=1}^n \frac{\partial N_k}{\partial X}\theta_k\right)\right.$$
$$\left. + \left(\sum_{j=1}^n V_j N_j\right)\left(\sum_{k=1}^n \frac{\partial N_k}{\partial Y}\theta_k\right)\right] d\Omega + \frac{1}{RePr}\sum_{j=1}^n \left(\int_\Omega \nabla N_i \cdot \nabla N_j \, d\Omega\right)\theta_j = F_\theta.$$

Defining,

$$M_{ij} = \int_\Omega N_i N_j d\Omega, \qquad K_{ij} = \int_\Omega (\nabla N_i . \nabla N_j) d\Omega,$$

Here, The non linear convective contribution is linearized and denoted compactly by the convection matrix $N(\theta)$. So, the semi discrete matrix form of energy equation can be written as,

$$M\frac{\partial\theta}{\partial T} + N(\theta)\theta + \frac{1}{RePr}K\theta = F_\theta. \tag{3.26}$$

Here in Eq.3.23-Eq.3.26, F_u, F_v, F_w, F_θ are the load vectors that are obtained from boundary integrals after the use of Green's theorem. These boundary conditions include the effects of natural boundary conditions and boundary fluxes. The Dirichlet boundary conditions are applied to all walls of the cavity for this present problem. Thus, the boundary integrals become zero when we apply the essential boundary conditions: $F_u = F_v = F_w = F_\theta = 0$..

3.3.3 Assembly of the Global System of Equations

The finite element discretizations of the governing equations leads to a set of algebraic equations that are defined at the level of finite elements. All the element equations are collected to form the global system of equations for the velocity, pressure, micro-rotation, and temperature fields. The set of finite element equations can be expressed as

$$M\frac{\partial U}{\partial T} + N(U)U - G_xP + \frac{1}{Re}KU - \frac{K}{Re}C_yW = 0. \tag{3.27}$$

$$M\frac{\partial V}{\partial T} + N(V)V - G_yP + \frac{1}{Re}KV + \frac{K}{Re}C_xW - B\theta = 0. \tag{3.28}$$

$$M\frac{\partial W}{\partial T} + N(W)W + \frac{1}{Re}\left(1+\frac{K}{2}\right)KW - \frac{2K}{E_rRe}(C_{vx}V - C_{uy}U - 2SW) = 0. \tag{3.29}$$

$$M\frac{\partial\theta}{\partial T} + N(\theta)\theta + \frac{1}{RePr}K\theta = 0. \tag{3.30}$$

subject to the incompressibility constraint,

$$D_xU + D_yV = 0. \tag{3.31}$$

3.3.4 Temporal Discretization using the Backward Eular Method

After assembling, The finite element system can be compactly written as the global finite element system:

$$M\frac{\partial X}{\partial T} + \mathbf{R}(\mathbf{X}) = \mathbf{F}, \tag{3.32}$$

M is the global mass matrix, $\mathbf{R(X)}$ contains the connective, diffusion, pressure coupling and micropolar coupling terms and $\mathbf{F}$ is the load vector. Let combining all unknown variables into a single solution vector,

$$\mathbf{X} = \begin{Bmatrix} U \\ V \\ P \\ W \\ \theta \end{Bmatrix}, \tag{3.33}$$

To advance the solution in time, the Backward Euler scheme is employed. Let T^n and T^{n+1} denote two consecutive time levels separated by a time step ΔT. The temporal derivative is approximated by,

$$\left.\frac{dX}{dT}\right|^{n+1} \approx \frac{X^{n+1} - X^n}{\Delta T}, \tag{3.34}$$

where X^n and X^{n+1} represent the solution vectors at times T^n and T^{n+1}, respectively. Substituting Eq.3.34 into Eq.3.32 yields,

$$M\left(\frac{X^{n+1} - X^n}{\Delta T}\right) + R(X^{n+1}) = F^{n+1}, \tag{3.35}$$

Multiplying Eq. (3.35) by ΔT, gets

$$MX^{n+1} - MX^n + \Delta T\, R(X^{n+1}) = \Delta T\, F^{n+1}. \tag{3.36}$$

Rearranging the terms gives

$$MX^{n+1} + \Delta T\, R(X^{n+1}) = MX^n + \Delta T\, F^{n+1}. \tag{3.37}$$

The fully discrete finite element formulation can therefore be expressed as

$$A^{n+1}X^{n+1} = b^n, \tag{3.38}$$

where $A^{n+1} = M + \Delta T\, R$, is the global coefficient matrix and $b^n = MX^n + \Delta T\, F^{n+1}$, is the right-hand-side vector. This is the nonlinear algebraic system to be solved at each time step in order to calculate the velocity, pressure, microrotation and temperature fields, as described by Eq.3.38. =Application of the Backward Euler Scheme to the Governing Equations Using Eq.3.34, the temporal derivatives are approximated as:

$$\frac{\partial U}{\partial T} \approx \frac{U^{n+1} - U^n}{\Delta T},$$
$$\frac{\partial V}{\partial T} \approx \frac{V^{n+1} - V^n}{\Delta T},$$

$$\frac{\partial W}{\partial T} \approx \frac{W^{n+1} - W^n}{\Delta T},$$
$$\frac{\partial \theta}{\partial T} \approx \frac{\theta^{n+1} - \theta^n}{\Delta T}.$$

Application to the X-Momentum Equation: To illustrate the temporal discretization procedure, consider the semi-discrete X-momentum equation

$$M\frac{\partial U}{\partial T} + N(U)U - G_x P + \frac{1}{Re}KU - \frac{K}{Re}C_y W = 0.$$

Applying the Backward Euler approximation, becomes

$$M\left(\frac{U^{n+1} - U^n}{\Delta T}\right) + N(U^{n+1})U^{n+1} - G_x P^{n+1} + \frac{1}{Re}KU^{n+1} - \frac{K}{Re}C_y W^{n+1} = 0.$$

Multiplying by ΔT gives,

$$MU^{n+1}-MU^{n}+\Delta T\, N(U^{n+1})U^{n+1}-\Delta T\, G_x P^{n+1}+\frac{\Delta T}{Re}KU^{n+1}-\frac{K\Delta T}{Re}C_y W^{n+1}=0.$$

Rearranging,

$$\left(M+\Delta T\, N(U^{n+1})+\frac{\Delta T}{Re}K\right)U^{n+1}-\Delta T\, G_x P^{n+1}-\frac{K\Delta T}{Re}C_y W^{n+1}=MU^{n}. \quad (3.39)$$

The same operation is performed with the Y-momentum, the microrotation and the energy equations to get their fully-discrete forms.

Y-Momentum Equation

$$M\left(\frac{V^{n+1}-V^{n}}{\Delta T}\right)+N(V^{n+1})V^{n+1}-G_y P^{n+1}+\frac{1}{Re}KV^{n+1}+\frac{K}{Re}C_x W^{n+1}-B\theta^{n+1}=0.$$

$$\begin{aligned}\Rightarrow &\left(M+\Delta T\, N(V^{n+1})+\frac{\Delta T}{Re}K\right)V^{n+1}\\ &-\Delta T\, G_y P^{n+1}+\frac{K\Delta T}{Re}C_x W^{n+1}-\Delta T\, B\theta^{n+1}=MV^{n}. \end{aligned} \quad (3.40)$$

Microrotation Equation

$$\begin{aligned}&M\left(\frac{W^{n+1}-W^{n}}{\Delta T}\right)+N(W^{n+1})W^{n+1}+\frac{1}{Re}\left(1+\frac{K}{2}\right)KW^{n+1}\\ &+\frac{2K}{Er\,Re}C_x V^{n+1}-\frac{2K}{Er\,Re}C_y U^{n+1}-\frac{4K}{Er\,Re}MW^{n+1}=0.\end{aligned}$$

$$\begin{aligned}\Rightarrow &\left[M+\Delta T\, N(W^{n+1})+\frac{\Delta T}{Re}\left(1+\frac{K}{2}\right)K-\frac{4K\Delta T}{Er\,Re}M\right]W^{n+1}\\ &+\frac{2K\Delta T}{Er\,Re}C_x V^{n+1}-\frac{2K\Delta T}{Er\,Re}C_y U^{n+1}=MW^{n}. \end{aligned} \quad (3.41)$$

Energy Equation

$$M\left(\frac{\theta^{n+1}-\theta^{n}}{\Delta T}\right)+N(\theta^{n+1})\theta^{n+1}+\frac{1}{Re\,Pr}K\theta^{n+1}=0.$$

$$\Rightarrow \left(M + \Delta T\, N(\theta^{n+1}) + \frac{\Delta T}{Re\, Pr} K \right) \theta^{n+1} = M\theta^{n}. \tag{3.42}$$

Continuity Equation Since the continuity equation does not contain a temporal derivative, it remains unchanged:

$$D_x U^{n+1} + D_y V^{n+1} = 0. \tag{3.43}$$

The implicitness of the Backward Euler scheme gives its remarkable numeric stability and this is especially useful to solve the present transient mixed convection micropolar flow problem.

3.4 Numerical Solution Algorithm

The numerical solution of the governing equations is derived by applying the implicit Backward Euler time integration scheme and Galerkin finite element method. The following steps are used in the present study for the computational procedure:

i. Set up the computational mesh for the square cavity.
ii. Specify the finite element spaces of velocity, pressure, microrotation and temperature.
iii. Compute global finite element matrices and vectors.
iv. Use the prescribed initial and boundary conditions.
v. Use the Backward Euler method to discretize the governing equations in time.
vi. At each time step, solve the coupled system of algebraic equations for the unknown variables.
vii. Repeat the process until the solution variables converge to within the specified level or until the desired simulation time.

Numerical procedure was simulated in FreeFEM++ to get numerical distribution of velocity, pressure, microrotation and temperature distributions in computation.

3.5 Implementation in FreeFEM++

FreeFEM++ was used to implement the finite element formulation presented in the previous sections. The computational domain was triangulated using unstructured triangular finite elements, while finite element spaces for velocity, pressure, microrotation and temperature were chosen. The variational formulation was used in FreeFEM++ to implement the weak form of the governing equations. The matrices and vectors for the element were constructed to get the global system of equations. Next the computational domain was subjected to the prescribed initial and boundary conditions. The system of coupled algebraic equations obtained were then discretized in time using the implicit Backward Euler scheme. The velocity, pressure, microrotation and temperature fields were obtained at each time step by solving the assembled system. The convergence criterion was used as prescription to repeat this procedure until the convergence was reached. The developed FreeFEM++ implementation was used to examine the nature of the mixed convection micropolar flow and heat transfer inside the square cavity for different values of the dimensionless parameters of the problem. The numerical results achieved on the implementation are included and discussed in the next chapter.

3.5.1 Numerical Procedure for implementation in FreeFEM++

The following numerical procedure used to obtain the solution:

i. Specify Re, Gr, Pr, K, and Er.

ii. Set the time step Δt and initialize $T = 0$.

iii. Define the computational geometry and boundary conditions.

iv. Generate the triangular computational mesh.

v. Define the finite element spaces.

vi. Initialize the solution fields.

vii. Formulate the weak form of the energy equation.

viii. Formulate the weak forms of the momentum and microrotation equations.

ix. Apply the prescribed boundary conditions.

x. Solve the temperature equation.

xi. Update the temperature field.

xii. Solve the coupled momentum, pressure, microrotation system.

xiii. Update the velocity and microrotation fields.

xiv. Advance the time by Δt.

xv. Repeat the procedure for the prescribed number of time steps.

xvi. Post process the numerical results.

Chapter 4

Results and Discussion

4.1 Validation of Numerical Results

To validate the accuracy and reliability of the developed finite element formulation, the classical lid-driven cavity flow problem is considered as a benchmark test case. The present mathematical model is reduced to the standard incompressible Navier–Stokes formulation by neglecting the thermal transport effects, excluding the microrotation momentum equation, and removing the mixed convection terms. Under these assumptions, the governing equations represent the conventional lid-driven cavity problem, which has been extensively studied in the literature.

The numerical results obtained from the present `FreeFEM++` implementation are compared with the well-established benchmark solutions reported by Ghia et al. [35]. Tables 4.1 and 4.2 present the comparison of the computed velocity components with the reference data of Ghia et al. [35].

The horizontal velocity component U is evaluated along the vertical centerline ($X = 0.5$), whereas the vertical velocity component V is evaluated along the horizontal centerline ($Y = 0.5$) for Reynolds numbers $Re = 100$, and 400. In addition to direct comparison, absolute errors between the present results and benchmark values are computed as:

$$\text{Error} = |u_{\text{Ghia}} - u_{\text{present}}|,$$

$$\text{Error} = |v_{\text{Ghia}} - v_{\text{present}}|.$$

It can be observed from Table 4.1 that the present predictions of the horizontal velocity profile closely follow the benchmark solutions for all considered Reynolds numbers. The characteristic change in the velocity distribution with increasing Reynolds number is accurately captured. In particular, the formation of the primary recirculating vortex and the associated variation of velocity near the cavity walls are correctly represented.

The small differences between the present results and the reference values occur mainly in the higher Reynolds number cases, where stronger convection effects and sharper velocity gradients demand higher spatial resolution. Similarly, Table 4.2 demonstrates a very good agreement between the computed and benchmark vertical velocity profiles.

The locations corresponding to positive and negative velocity regions along the horizontal centerline are accurately reproduced for all Reynolds numbers. The maximum deviations between the present calculations and Ghia et al. [35] remain within an acceptable range, confirming the capability of the finite element discretization to resolve the complex flow features associated with the lid-driven cavity configuration. The close agreement observed in both velocity components confirms that the present numerical framework can accurately reproduce the classical cavity flow behavior in the limiting case.

Since the benchmark problem represents a simplified version of the developed coupled model, this validation provides confidence in the implementation of the spatial discretization, time integration procedure, and solution algorithm. Therefore, the extended formulation incorporating thermal effects, microrotation dynamics, and mixed convection phenomena can be considered a reliable generalization of the classical lid-driven cavity problem.

TABLE 4.1: Validation of U-velocity with absolute error compared to Ghia et al. [35].

Y	Re = 100			Re = 400		
	Ghia	Present	Error	Ghia	Present	Error
0.9766	0.841230	0.841016	0.000214	0.758370	0.758012	0.000358
0.7344	0.003320	0.003287	0.000033	0.162560	0.162843	0.000283
0.6172	-0.136410	-0.136082	0.000328	0.021350	0.021612	0.000262
0.5000	-0.205810	-0.205274	0.000536	-0.114770	-0.115126	0.000356
0.2813	-0.156620	-0.156937	0.000317	-0.327260	-0.327841	0.000581
0.1016	-0.064340	-0.064726	0.000386	-0.146120	-0.146593	0.000473

TABLE 4.2: Validation of V-velocity with absolute error compared to Ghia et al. [35].

X	Re = 100			Re = 400		
	Ghia	Present	Error	Ghia	Present	Error
0.0703	0.100910	0.101238	0.000328	0.197130	0.197684	0.000554
0.2344	0.175270	0.174914	0.000356	0.301740	0.302185	0.000445
0.5000	0.054540	0.054286	0.000254	0.051860	0.052147	0.000287
0.8047	-0.245330	-0.244926	0.000404	-0.385980	-0.385472	0.000508
0.9063	-0.169140	-0.169586	0.000446	-0.238270	-0.238811	0.000541
0.9688	-0.059060	-0.059421	0.000361	-0.121460	-0.121892	0.000432

The results presented in Tables 4.1 and 4.2 indicate that the present finite element solution exhibits excellent agreement with the benchmark data. For the U-velocity profile along the vertical centerline, the absolute error remains of the order 10^{-4} to 10^{-3} across all nodal locations and Reynolds numbers considered. Similarly, for the V-velocity profile along the horizontal centerline, the error magnitude remains consistently small, confirming the accuracy of the numerical approximation.

The slightly larger deviations observed at certain interior points are expected in finite element simulations of convection-dominated flows and can be attributed to discretization effects, mesh resolution, and numerical diffusion inherent in stabilized

time-dependent schemes. Despite these minor discrepancies, the overall agreement remains very strong, particularly in capturing key flow features such as the primary vortex structure and velocity reversal regions.

The small error levels demonstrate that the implemented Galerkin finite element formulation in `FreeFEM++` is both stable and accurate. This confirms the correctness of the spatial discretization, time integration scheme, and boundary condition implementation. Moreover, the successful reproduction of the benchmark results provides strong validation of the computational framework before extending it to more complex physics involving thermal effects, micropolar behavior, and mixed convection phenomena.

4.2 Calculations of Results

In this section the computed results are dicsussed in detail. Figure 4.1 illustrates the temperature distribution within the computational domain for various values of the Prandtl number (Pr) and the micropolar coupling parameter (K). The remaining dimensionless parameters are fixed at $Re = 10$, $Gr = 5$, and $Er = 0.3$. The thermal field is generated by the heated section located on the lower portion of the left wall, while the remaining boundaries are thermally insulated except for the outlet. Consequently, heat initially diffuses from the heated wall into the cavity and is subsequently transported by the combined effects of forced and buoyancy-driven convection.

For the lowest Prandtl number ($Pr = 0.3$), shown in Figures 4.1(a) and 4.1(b), the temperature contours are widely distributed throughout the cavity. Since the thermal diffusivity is inversely proportional to the Prandtl number through the diffusion coefficient $\frac{1}{RePr}$ appearing in the energy equation, a smaller value of Pr corresponds to relatively high thermal diffusivity. Heat therefore spreads rapidly away from the heated wall, producing smooth temperature gradients and allowing thermal energy to penetrate a large portion of the enclosure. The isotherms exhibit broad spacing, indicating relatively weak thermal gradients.

As the Prandtl number increases to $Pr = 0.7$ (Figures 4.1(c) and 4.1(d)), thermal diffusion decreases and convective transport becomes relatively more dominant. Consequently, the isotherms become more concentrated near the heated region, indicating that heat remains localized for a longer distance before diffusing into the surrounding fluid. The thermal boundary layer becomes more distinct, while the temperature gradients near the heated wall become steeper. This behaviour is characteristic of fluids with moderate Prandtl numbers, where momentum diffuses more rapidly than heat.

A further increase to $Pr = 1.3$ (Figures 4.1(e) and 4.1(f)) intensifies this trend. The temperature contours become increasingly compressed near the heat source, while the thermal field occupies a comparatively smaller region of the cavity. The higher Prandtl number significantly reduces thermal diffusivity, restricting the conduction of heat into the interior and resulting in a thinner thermal boundary layer. Consequently, larger temperature gradients develop adjacent to the heated wall, which generally correspond to enhanced local heat transfer rates.

The influence of the micropolar parameter can be assessed by comparing each pair of figures having identical Prandtl numbers. Increasing the coupling parameter from $K = 0$ to $K = 5.5$ produces only modest changes in the overall temperature field. The general structure of the isotherms remains nearly unchanged, indicating that the temperature distribution is primarily governed by the balance between convection and thermal diffusion rather than by the microrotation effects. Nevertheless, slight distortions of the contours are noticeable, particularly in the interior of the enclosure, where the micropolar coupling alters the momentum field through the interaction between the linear and angular momentum equations. These modifications slightly redistribute the convective transport of heat without significantly changing the overall thermal pattern.

Overall, Figure 4.1 demonstrates that the Prandtl number exerts a much stronger influence on the thermal field than the micropolar parameter under the present flow conditions. Increasing Pr consistently produces thinner thermal boundary layers and stronger temperature gradients, whereas variations in K mainly induce

minor adjustments to the convective heat transport through their influence on the velocity field.

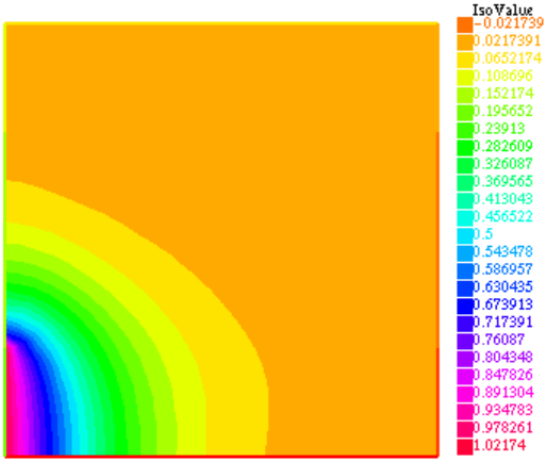
The observed behaviour follows directly from the nondimensional energy equation,

$$\frac{\partial \theta}{\partial T} + U\frac{\partial \theta}{\partial X} + V\frac{\partial \theta}{\partial Y} = \frac{1}{Re\,Pr}\left(\frac{\partial^2 \theta}{\partial X^2} + \frac{\partial^2 \theta}{\partial Y^2}\right). \tag{4.1}$$

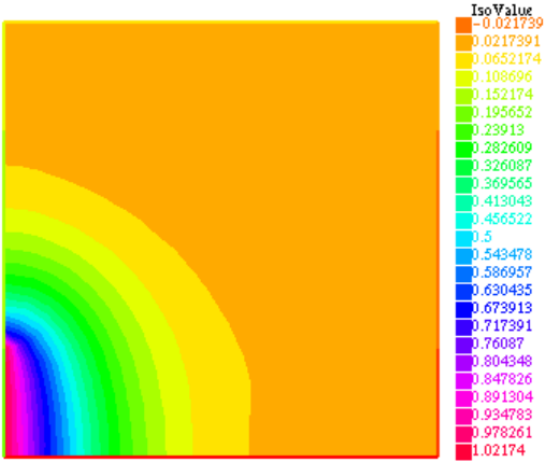
It is evident from the above equation that increasing the Prandtl number decreases the thermal diffusion coefficient $\frac{1}{RePr}$, thereby reducing thermal diffusion and confining heat closer to the heated wall. This results in thinner thermal boundary layers and steeper temperature gradients. On the other hand, the micropolar parameter K does not appear explicitly in the energy equation. Its influence is indirect through the momentum and microrotation equations, where it modifies the velocity components (U, V). Since convective heat transport depends on the velocity field, variations in K only produce secondary changes in the temperature distribution. This explains the relatively small differences observed between the cases corresponding to $K = 0$ and $K = 5.5$.

Figure 4.2 presents the temperature contours for different values of the Eringen parameter (Er), while keeping the remaining dimensionless parameters fixed at $Re = 10$, $K = 5.0$, $Gr = 5$, and $Pr = 0.3$. The Eringen parameter characterizes the micro-inertia of the microstructural elements of the micropolar fluid and governs the strength of the coupling between the microrotation field and the translational motion of the fluid. Its influence on the thermal field is therefore indirect through the modification of the velocity distribution, which subsequently alters the convective transport of heat.

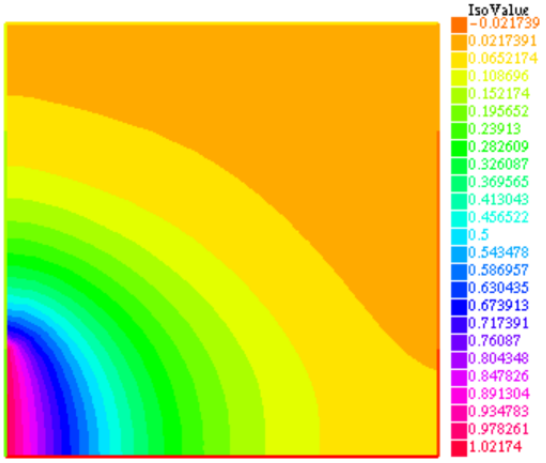
For the largest value, $Er = 0.3$ (Figure 4.2(a)), the temperature contours remain relatively smooth and nearly concentric around the heated section located on the lower part of the left wall. The thermal energy spreads predominantly by conduction with only moderate distortion caused by convection. The thermal boundary layer is relatively uniform, indicating a stable balance between heat diffusion and fluid motion.



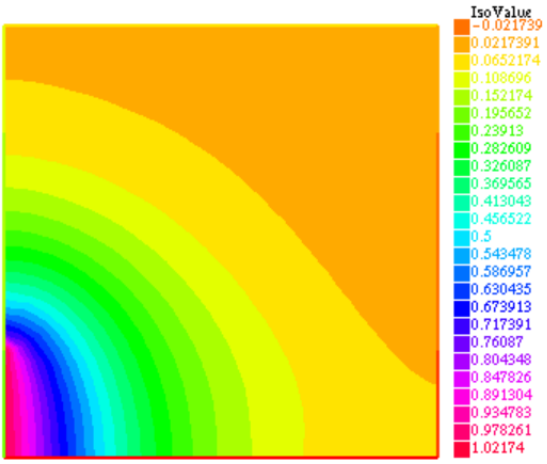
(a) $Pr = 0.3$ $K = 0$



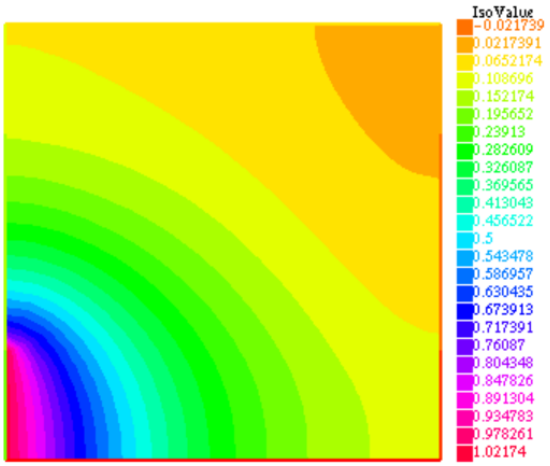
(b) $Pr = 0.3$ $K = 5.5$



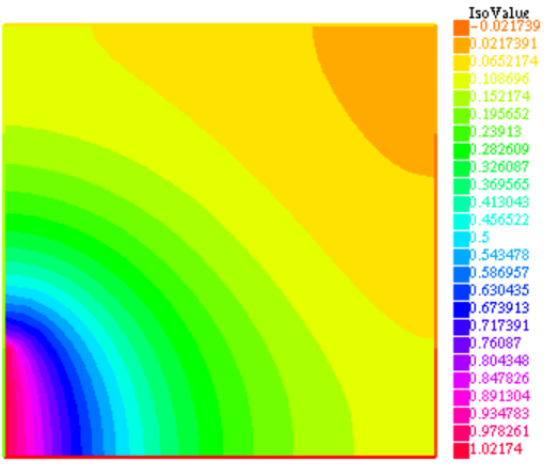
(c) $Pr = 0.7$ $K = 0$



(d) $Pr = 0.7$ $K = 5.5$



(e) $Pr = 1.3$ $K = 0$



(f) $Pr = 1.3$ $K = 5.5$

FIGURE 4.1: Temperature streamlines for varying values of the Prandtl number. Other parameters used are $Re = 10$, $Gr = 0.5$, $Er = 0.3$.

As the Eringen parameter decreases to $Er = 0.1$ (Figure 4.2(b)), the temperature contours begin to deform and extend further into the interior of the enclosure. The isotherms become asymmetric, indicating that convective transport is becoming more significant. The enhanced interaction between the microrotation and linear momentum modifies the flow circulation, causing heat to be transported farther away from the heated wall and producing a more elongated thermal plume.

A further reduction to $Er = 0.05$ (Figure 4.2(c)) produces a pronounced distortion of the temperature field. The isotherms exhibit a clear rotational structure that follows the primary circulation inside the cavity. The temperature contours are no longer nearly concentric but instead wrap around the recirculating flow, demonstrating that convection dominates over pure thermal diffusion. The heated fluid is carried deeper into the enclosure, resulting in greater mixing between the hot and cold fluid regions.

For the smallest value, $Er = 0.03$ (Figure 4.2(d)), the thermal plume becomes highly asymmetric and extends across a significant portion of the cavity. The temperature contours are strongly stretched and distorted, indicating vigorous convective transport. The heated fluid is advected rapidly by the circulating flow, leading to enhanced thermal mixing and a larger heated region within the enclosure. The increased deformation of the isotherms suggests a stronger interaction between the thermal and momentum fields under reduced micro-inertia.

The observed behaviour can be explained from the dimensionless microrotation equation,

$$\frac{\partial W}{\partial T} + U\frac{\partial W}{\partial X} + V\frac{\partial W}{\partial Y} = \frac{1}{Re}\left(1 + \frac{K}{2}\right)\nabla^2 W + \frac{2K}{Er\,Re}\left(\frac{\partial V}{\partial X} - \frac{\partial U}{\partial Y} - 2W\right). \quad (4.2)$$

The coupling term is inversely proportional to the Eringen parameter. Consequently, decreasing Er increases the magnitude of this coupling, thereby strengthening the interaction between the angular and linear momentum fields. The resulting modifications in the velocity distribution enhance convective heat transport, even though Er does not explicitly appear in the energy equation. Since the energy

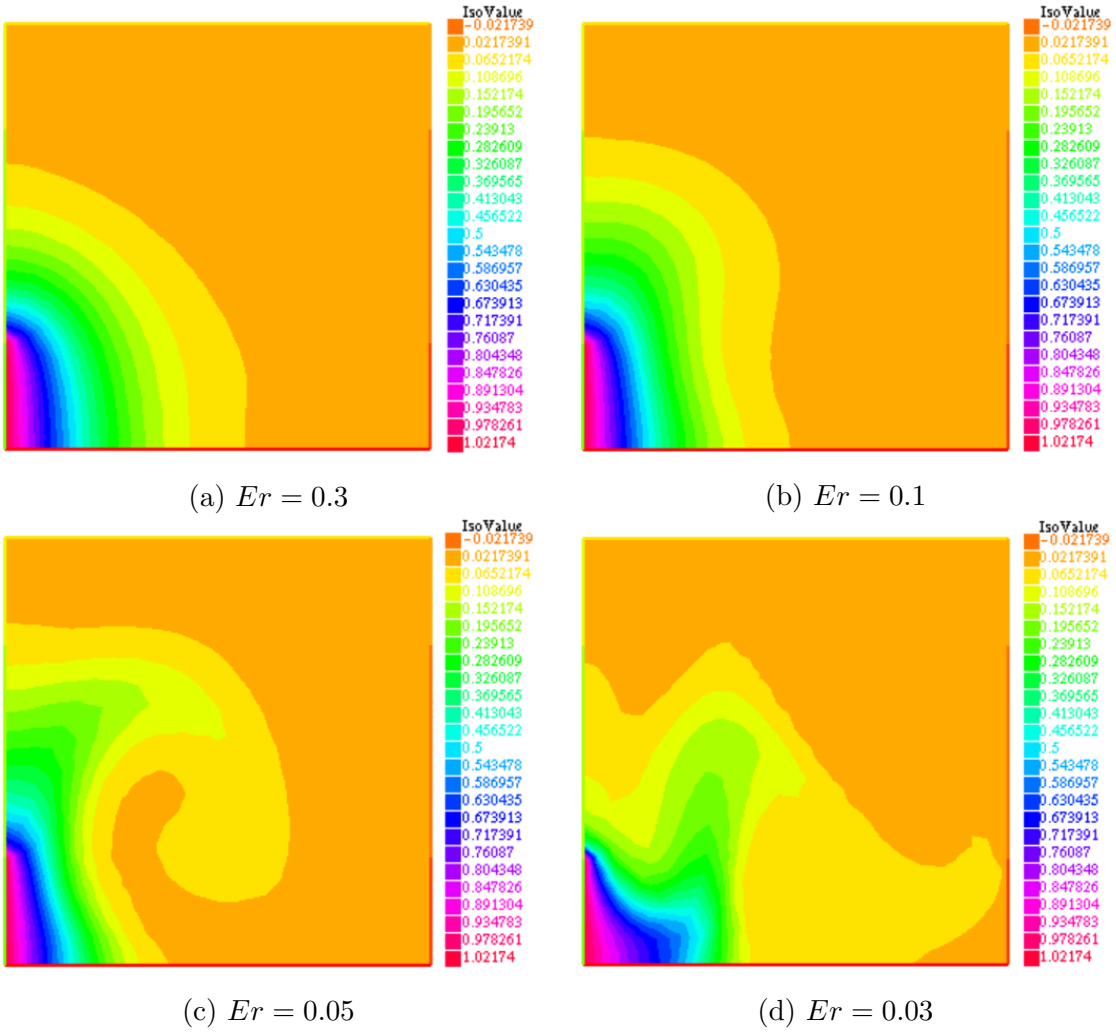
equation depends on the velocity components (U, V) through the convective terms, stronger flow circulation caused by smaller values of Er produces increasingly distorted temperature contours and improved thermal mixing.

Overall, Figure 4.2 demonstrates that reducing the Eringen parameter significantly enhances the influence of microrotation on the flow dynamics, leading to stronger convection, greater distortion of the thermal field, and more effective transport of heat throughout the enclosure.

An additional feature observed in Figure 4.2 is the progressive development and bending of the thermal plume as the Eringen parameter decreases. For $Er = 0.3$, the heated region remains localized near the heated section with relatively smooth and concentric isotherms, indicating that thermal diffusion is the dominant mode of heat transfer. However, as Er decreases to 0.1, 0.05, and finally 0.03, the thermal plume extends further into the cavity and gradually bends toward the interior following the primary recirculating flow. This behaviour signifies a transition from diffusion-dominated to convection-dominated heat transport, where the circulating fluid effectively advects thermal energy away from the heated wall. The enhanced plume penetration and increasing distortion of the isotherms demonstrate that the strengthened coupling between the microrotation and momentum fields intensifies the fluid circulation, thereby promoting more efficient thermal mixing and improving the overall distribution of heat throughout the enclosure.

Figure 4.3 presents the contours of the horizontal velocity component (U) for different values of the Reynolds number (Re), while keeping the remaining dimensionless parameters fixed at $Gr = 0.3$, $Pr = 0.3$, $K = 5.5$, and $Er = 0.3$. The Reynolds number represents the ratio of inertial forces to viscous forces and therefore plays a fundamental role in determining the flow structure within the enclosure. The horizontal velocity field is primarily generated by the moving lid located on the upper portion of the left wall, while buoyancy and micropolar effects further modify the flow through their coupling with the momentum equations.

For the lowest Reynolds number, $Re = 1$ (Figure 4.3(a)), viscous forces dominate the flow. Consequently, momentum diffuses smoothly throughout the cavity,



(a) $Er = 0.3$ (b) $Er = 0.1$

(c) $Er = 0.05$ (d) $Er = 0.03$

FIGURE 4.2: Temperature streamlines for varying values of the Eringen number. Other parameters used are $Re = 10$, $Gr = 0.5$, $Pr = 0.3$, $K = 5.5$

producing a relatively uniform distribution of the horizontal velocity. The contours exhibit gradual variations with broad spacing, indicating weak velocity gradients and a stable, diffusion-dominated flow. The influence of the moving lid extends over a large portion of the enclosure due to the strong viscous diffusion of momentum.

As the Reynolds number increases to $Re = 10$ (Figure 4.3(b)), inertial forces become more pronounced while the influence of viscosity decreases. The velocity contours become slightly more compressed near the moving lid and along the recirculating flow path, indicating the development of stronger velocity gradients. The momentum transported by the moving lid penetrates further into the cavity through convection, resulting in a more organized circulation pattern and increased

flow intensity.

A further increase to $Re = 100$ (Figure 4.3(c)) significantly alters the flow structure. The horizontal velocity contours become highly distorted and concentrated, particularly near the upper-left moving wall and the lower-right region of the cavity. The increased dominance of inertial forces promotes stronger circulation and enhances the transport of momentum throughout the enclosure. Localized regions of high positive and negative horizontal velocity become more evident, indicating intensified recirculation and increased shear within the flow. The appearance of a distinct low-velocity region in the interior of the cavity also suggests the formation of secondary flow structures resulting from the stronger interaction between the primary circulation and the stationary walls.

These observations can be explained from the dimensionless momentum equation governing the horizontal velocity,

$$\frac{\partial U}{\partial T} + U\frac{\partial U}{\partial X} + V\frac{\partial U}{\partial Y} = -\frac{\partial P}{\partial X} + \frac{1}{Re}\left(\frac{\partial^2 U}{\partial X^2} + \frac{\partial^2 U}{\partial Y^2}\right) + \frac{K}{Re}\frac{\partial W}{\partial Y}. \tag{4.3}$$

The viscous diffusion term is inversely proportional to the Reynolds number. Therefore, increasing Re reduces the diffusive transport of momentum while allowing the convective terms to dominate the flow dynamics. Although the micropolar coupling term also contains the factor $\frac{1}{Re}$, the enhanced convection associated with larger Reynolds numbers becomes the governing mechanism controlling the overall velocity distribution. As a result, sharper velocity gradients and stronger recirculation zones are observed at higher Reynolds numbers.

Another important feature visible in Figure 4.3 is the progressive concentration of the velocity contours near the moving lid and the downstream corner as the Reynolds number increases. At low Reynolds numbers, momentum diffuses uniformly across the cavity, producing relatively smooth contours. However, for $Re = 100$, the contours become compressed near the boundaries while the core region develops localized velocity extrema. This behaviour reflects the formation of thinner momentum boundary layers and stronger convective transport, indicating

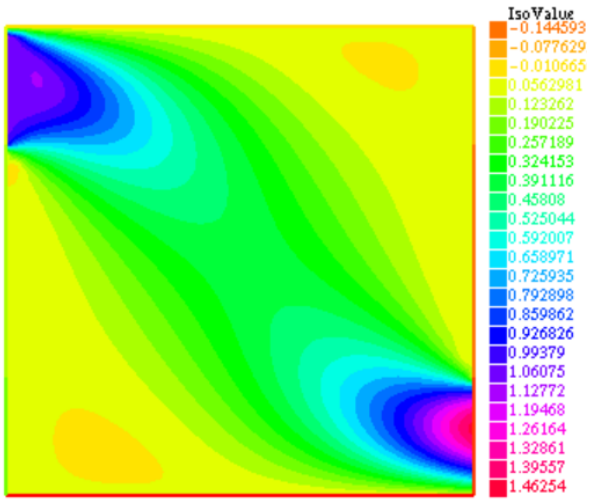
that inertia increasingly dominates over viscous diffusion. The enhanced circulation improves momentum transport throughout the enclosure while simultaneously generating more complex flow structures characteristic of mixed convection at moderate Reynolds numbers.

Figure 4.4 illustrates the contours of the microrotation velocity (W) for different values of the micropolar coupling parameter (K), while the remaining dimensionless parameters are fixed at $Re = 1.0$, $Gr = 0.5$, $Pr = 0.3$, and $Er = 0.3$. The micropolar parameter represents the coupling between the linear momentum and the angular momentum of the microstructural elements within the fluid. Increasing K strengthens this coupling, thereby influencing both the magnitude and distribution of the microrotation field throughout the enclosure.

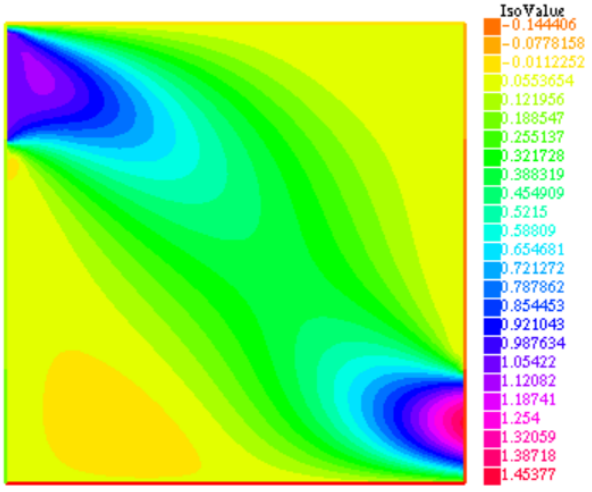
For the smallest value, $K = 0.5$ (Figure 4.4(a)), the microrotation field exhibits relatively small magnitudes and smooth contour distributions. The rotational motion of the microelements is confined to localized regions adjacent to the primary flow path, while the central portion of the cavity experiences comparatively weak angular motion. The gradual variation of the contours indicates that the rotational energy generated by the moving lid is only moderately transmitted into the interior of the enclosure.

As the micropolar parameter increases to $K = 5.5$ (Figure 4.4(b)), the intensity of the microrotation field increases considerably. The contours become more closely spaced, indicating stronger gradients of angular velocity. The regions of positive and negative microrotation expand further into the cavity, demonstrating that the rotational effects are no longer confined near the boundaries but penetrate deeper into the fluid domain. This behaviour reflects the stronger interaction between the translational motion of the fluid and the rotation of its microstructural elements.

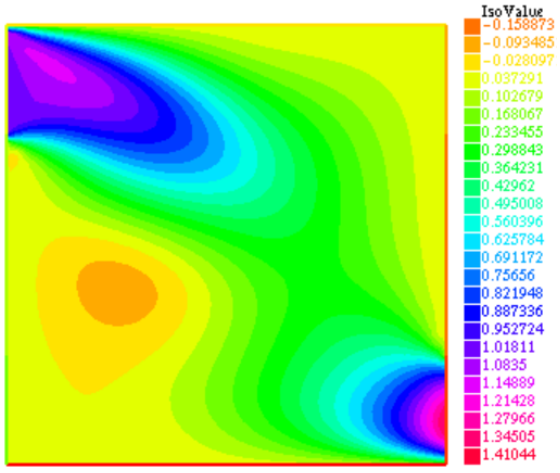
A further increase to $K = 7.5$ (Figure 4.4(c)) produces an even more pronounced enhancement of the microrotation field. The contour levels indicate significantly larger positive and negative values of W, while the regions of intense microrotation occupy a greater portion of the enclosure. The contours become increasingly compressed near the interfaces separating positive and negative angular velocities,



(a) $Re = 1$



(b) $Re = 10$



(c) $Re = 100$

FIGURE 4.3: U-velocity profiles for varying values of the Reynolds number. Other parameters used are $Gr = 0.5$, $Pr = 0.3$, $K = 5.5$, $Er = 0.3$.

signifying steeper microrotation gradients and stronger rotational interactions within the fluid. The enlarged regions of high microrotation indicate that rotational energy is effectively transported throughout the cavity as the coupling between the momentum and angular momentum equations becomes stronger.

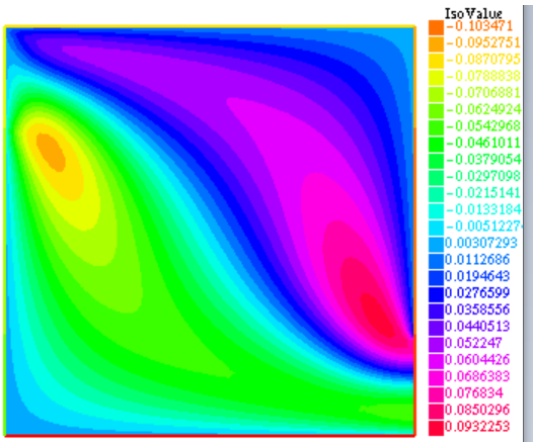
The observed behaviour is consistent with the governing dimensionless microrotation equation,

$$\frac{\partial W}{\partial T} + U\frac{\partial W}{\partial X} + V\frac{\partial W}{\partial Y} = \frac{1}{Re}\left(1 + \frac{K}{2}\right)\left(\frac{\partial^2 W}{\partial X^2} + \frac{\partial^2 W}{\partial Y^2}\right) + \frac{2K}{Er\,Re}\left(\frac{\partial V}{\partial X} - \frac{\partial U}{\partial Y} - 2W\right). \tag{4.4}$$

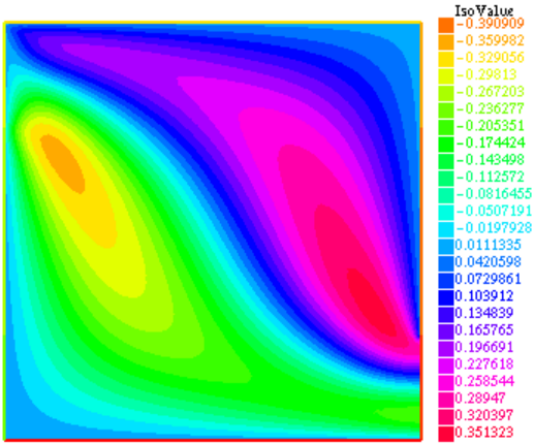
It is evident that the micropolar parameter appears explicitly in both the diffusion term and the coupling term of the microrotation equation. As K increases, the effective spin diffusion coefficient, $\left(1 + \frac{K}{2}\right)/Re$, becomes larger, facilitating the transport of angular momentum throughout the enclosure. Simultaneously, the coupling term, $\frac{2K}{ErRe}\left(\frac{\partial V}{\partial X} - \frac{\partial U}{\partial Y} - 2W\right)$, becomes stronger, resulting in a more efficient transfer of energy between the translational and rotational motions of the fluid. Consequently, both the magnitude and spatial extent of the microrotation field increase with increasing values of K.

Another noticeable feature of Figure 4.4 is the progressive enlargement of the positive and negative microrotation regions as K increases. The contour bands become more elongated along the primary circulation path, indicating that the rotating microelements are increasingly influenced by the global flow field rather than remaining confined near the moving boundary. This enhanced rotational transport promotes stronger interaction between adjacent fluid layers, which can significantly influence the momentum transport characteristics of micropolar fluids. Overall, the results demonstrate that the micropolar coupling parameter is one of the dominant factors controlling the angular velocity distribution and the rotational dynamics within the enclosure.

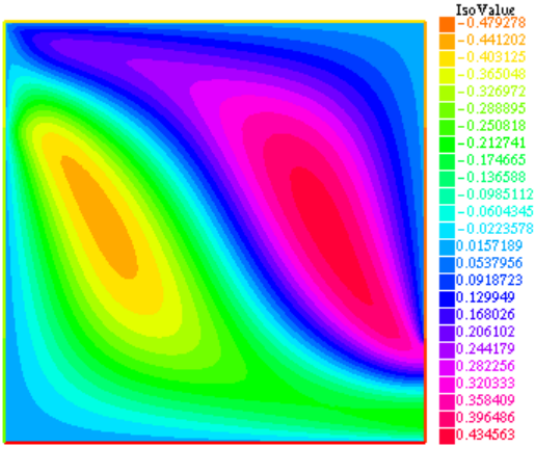
Figure 4.5 presents the contours of the microrotation velocity (W) for different



(a) $K = 0.5$



(b) $K = 5.5$



(c) $K = 7.5$

FIGURE 4.4: Microrotation velocity profiles for varying values of the Micropolar parameter. Other parameters used are $Re = 1.0$, $Gr = 0.5$, $Pr = 0.3$, $K = 0.005$, $Er = 0.3$.

values of the Eringen parameter (Er), while the remaining dimensionless parameters are fixed at $Re = 1.0$, $K = 5.0$, $Gr = 0.5$, and $Pr = 0.3$. The Eringen parameter

represents the normalized micro-inertia of the suspended microstructural elements and plays an important role in controlling the interaction between the angular and translational motions of the fluid. Since Er appears in the denominator of the coupling term in the microrotation equation, variations in Er directly influence the strength of the rotational response of the fluid microelements.

For the smallest value, $Er = 0.3$ (Figure 4.5(a)), the microrotation field exhibits the largest magnitude, with well-developed regions of positive and negative angular velocity extending throughout the enclosure. The contour bands are closely spaced near the interfaces separating opposite rotational directions, indicating steep gradients of microrotation and strong rotational activity within the fluid. The rotating microelements are strongly coupled with the velocity field, resulting in an intense exchange of angular and linear momentum.

As the Eringen parameter increases to $Er = 1.3$ (Figure 4.5(b)), the magnitude of the microrotation velocity decreases noticeably. Although the overall contour pattern remains similar, the regions of maximum positive and negative microrotation become smaller and the contour spacing becomes slightly wider. This indicates a reduction in the intensity of angular motion and weaker rotational interactions between neighboring fluid particles. The decrease in microrotation intensity also implies that the influence of the rotating microelements on the overall flow becomes less significant.

A further increase to $Er = 3.3$ (Figure 4.5(c)) continues this trend. The microrotation contours become even smoother, with reduced peak values and less pronounced gradients throughout the enclosure. The regions of strong angular velocity shrink further, while the central portion of the cavity exhibits relatively weak rotational motion. These observations indicate that larger values of the Eringen parameter suppress the rotational response of the microelements, resulting in a more uniform distribution of microrotation.

The observed behaviour can be explained using the dimensionless microrotation equation,

$$\frac{\partial W}{\partial T} + U\frac{\partial W}{\partial X} + V\frac{\partial W}{\partial Y} = \frac{1}{Re}\left(1 + \frac{K}{2}\right)\left(\frac{\partial^2 W}{\partial X^2} + \frac{\partial^2 W}{\partial Y^2}\right) + \frac{2K}{Er\,Re}\left(\frac{\partial V}{\partial X} - \frac{\partial U}{\partial Y} - 2W\right). \tag{4.5}$$

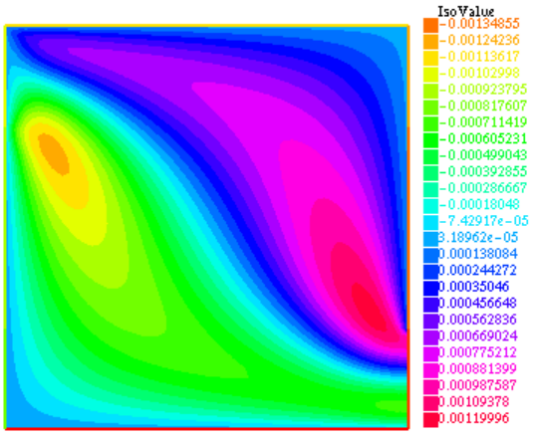
It is evident from the above equation that the coupling term is inversely proportional to the Eringen parameter. Consequently, increasing Er reduces the coefficient $\frac{2K}{ErRe}$, thereby weakening the interaction between the fluid vorticity and the microrotation field. As a result, less rotational energy is transferred from the translational motion of the fluid to the microstructural elements, leading to smaller values of the angular velocity throughout the enclosure. Although the spin diffusion term remains unchanged with respect to Er, the weakened coupling substantially reduces the overall intensity of the microrotation field.

Another important feature observed in Figure 4.5 is that the overall structure of the microrotation contours remains nearly unchanged as Er increases, while only their magnitude decreases. This indicates that the Eringen parameter primarily controls the strength of the rotational response rather than altering the fundamental flow topology. The locations of the positive and negative microrotation regions remain nearly identical for all cases, demonstrating that the global circulation pattern is governed mainly by the cavity geometry and boundary conditions, whereas the Eringen parameter regulates the extent to which the microstructural elements participate in the flow. Therefore, increasing Er suppresses the rotational activity of the microelements and reduces the coupling between the angular and translational momentum, resulting in a weaker microrotation field throughout the enclosure.

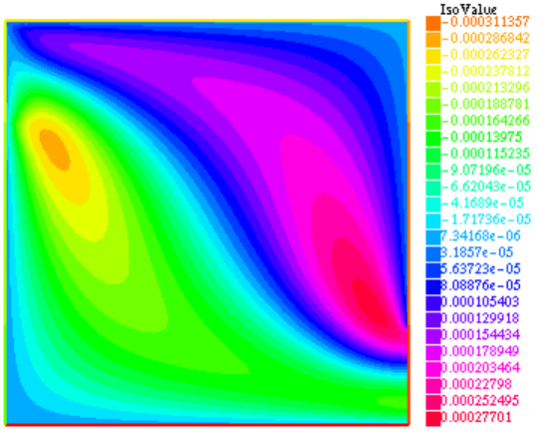
TABLE 4.3: Variation of W at different locations for different values of Eringen number Er. Other parameters are $Re = 1.0$, $Gr = 0.5$, $Pr = 0.3$, $K = 0.005$.

Er	$W(-0.25, 0.0)$	$W(0.0, 0.0)$	$W(0.35, 0.0)$
0.3	-0.000942929	-7.19008×10^{-5}	0.00091695
1.3	-0.000217819	-1.66222×10^{-5}	0.000211771
3.3	-8.58234×10^{-5}	-6.55025×10^{-6}	8.34368×10^{-5}
5.3	-5.34396×10^{-5}	-4.07878×10^{-6}	5.1953×10^{-5}
7.3	-3.87994×10^{-5}	-2.96142×10^{-6}	3.77199×10^{-5}

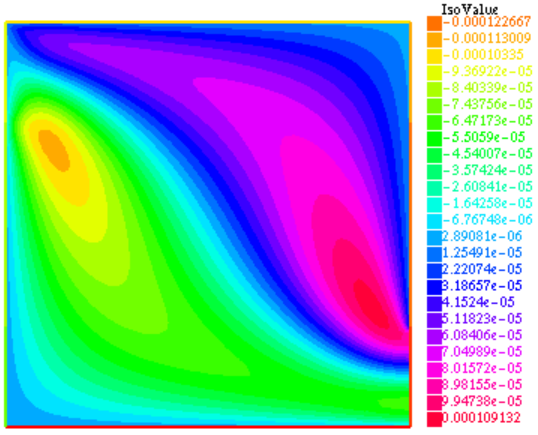
Table 4.3 presents the variation of the microrotation velocity (W) at three rep-



(a) $Er = 0.3$



(b) $Er = 1.3$



(c) $Er = 3.3$

FIGURE 4.5: Microrotation velocity profiles for varying values of the Eringen number. Other parameters used are $Re = 1.0$, $Gr = 0.5$, $Pr = 0.3$, $K = 0.005$, $Er = 3.3$.

resentative locations along the horizontal centreline of the enclosure for different values of the Eringen parameter (Er). The remaining parameters are fixed at

$Re = 1.0$, $Gr = 0.5$, $Pr = 0.3$, and $K = 0.005$. The selected locations, namely $(-0.25, 0.0)$, $(0.0, 0.0)$, and $(0.35, 0.0)$, represent the left, central, and right portions of the cavity, respectively, thereby providing a quantitative measure of the influence of the Eringen parameter on the microrotation field.

It is evident that the magnitude of the microrotation velocity decreases consistently with increasing values of the Eringen parameter at all three locations. At the left location, $W(-0.25, 0.0)$ decreases from -9.42929×10^{-4} for $Er = 0.3$ to -3.87994×10^{-5} for $Er = 7.3$, representing a substantial reduction in the rotational intensity. A similar trend is observed at the cavity centre, where the microrotation decreases from -7.19008×10^{-5} to -2.96142×10^{-6}, while at the right location, $W(0.35, 0.0)$ decreases from 9.16950×10^{-4} to 3.77199×10^{-5}. The nearly symmetric reduction in magnitude at the left and right locations indicates that the influence of the Eringen parameter is uniformly distributed throughout the enclosure.

The reduction in microrotation with increasing Er can be explained from the governing microrotation equation,

$$\frac{\partial W}{\partial T} + U\frac{\partial W}{\partial X} + V\frac{\partial W}{\partial Y} = \frac{1}{Re}\left(1 + \frac{K}{2}\right)\nabla^2 W + \frac{2K}{Er\,Re}\left(\frac{\partial V}{\partial X} - \frac{\partial U}{\partial Y} - 2W\right).$$

The coupling coefficient $\frac{2K}{ErRe}$ is inversely proportional to the Eringen parameter. Therefore, increasing Er weakens the interaction between the fluid vorticity and the rotational motion of the microstructural elements, resulting in a smaller transfer of angular momentum from the linear flow to the microrotation field. Consequently, the magnitude of W decreases throughout the enclosure as the rotational response of the microelements becomes progressively weaker.

Another noteworthy observation is that the sign of the microrotation remains unchanged at each monitoring location despite the variation in Er. The left side of the enclosure consistently exhibits negative microrotation, whereas the right side maintains positive values, while the magnitude at the cavity centre remains comparatively small. This indicates that the Eringen parameter primarily affects the intensity of the rotational motion without altering the overall rotational

direction established by the global circulation within the cavity. Hence, increasing the Eringen parameter suppresses the angular velocity of the microelements while preserving the overall structure of the microrotation field.

TABLE 4.4: Variation of W at different locations for different values of micropolar coupling parameter K.

K	$W(-0.25, 0.0)$	$W(0.0, 0.0)$	$W(0.35, 0.0)$
0.005	-0.000986047	-7.19008$\times 10^{-5}$	0.00091695
0.05	-0.00955441	-0.000693269	0.00889931
0.5	-0.0732078	-0.00508015	0.0689674
1.5	-0.149005	-0.0097433	0.140918
3.5	-0.236135	-0.0154803	0.215496
5.5	-0.323915	-0.0234727	0.275811
7.5	-0.45943	-0.0396627	0.353511

Table 4.4 presents the variation of the microrotation velocity (W) at three representative locations along the horizontal centreline of the enclosure for different values of the micropolar coupling parameter (K). The remaining parameters are kept fixed throughout the computations. The selected monitoring points, namely $(-0.25, 0.0)$, $(0.0, 0.0)$, and $(0.35, 0.0)$, correspond to the left, central, and right regions of the cavity, respectively, allowing a quantitative assessment of the influence of the micropolar parameter on the rotational motion of the fluid microelements.

It is observed that increasing the micropolar parameter K significantly enhances the magnitude of the microrotation velocity at all monitoring locations. At the left position, $W(-0.25, 0.0)$ increases in magnitude from -9.86047×10^{-4} for $K = 0.005$ to -4.59430×10^{-1} for $K = 7.5$. Similarly, the microrotation at the cavity centre increases from -7.19008×10^{-5} to -3.96627×10^{-2}, while at the right position, $W(0.35, 0.0)$ increases from 9.16950×10^{-4} to 3.53511×10^{-1}. These results demonstrate that even moderate increases in the micropolar coupling parameter produce a substantial amplification of the angular velocity throughout the enclosure.

This behaviour is consistent with the governing microrotation equation,

$$\frac{\partial W}{\partial T} + U\frac{\partial W}{\partial X} + V\frac{\partial W}{\partial Y} = \frac{1}{Re}\left(1 + \frac{K}{2}\right)\nabla^2 W + \frac{2K}{Er\,Re}\left(\frac{\partial V}{\partial X} - \frac{\partial U}{\partial Y} - 2W\right).$$

It is evident that the micropolar parameter appears explicitly in both the spin-diffusion term and the coupling term. As K increases, the effective spin diffusion coefficient, $\left(1 + \frac{K}{2}\right)/Re$, becomes larger, allowing the rotational motion of the microelements to spread more efficiently throughout the fluid domain. Simultaneously, the coupling coefficient $\frac{2K}{ErRe}$ increases linearly with K, strengthening the interaction between the fluid vorticity and the microrotation field. Consequently, more angular momentum is transferred from the translational motion of the fluid to the rotational motion of the suspended microelements, resulting in a pronounced increase in the microrotation velocity.

Another important observation is that the increase in microrotation is nearly symmetric about the cavity centre. The left monitoring point consistently exhibits negative values, whereas the right monitoring point maintains positive values of comparable magnitude. Meanwhile, the microrotation at the cavity centre remains relatively small because this region experiences weaker local rotational effects compared with the regions adjacent to the primary circulation. The preservation of the sign of W at all monitoring locations indicates that increasing K intensifies the rotational strength without altering the direction of the local angular motion.

Overall, Table 4.4 clearly demonstrates that the micropolar coupling parameter is one of the dominant governing parameters controlling the rotational dynamics of the flow. Larger values of K considerably strengthen the exchange of angular and linear momentum, thereby increasing the rotational activity of the microstructural elements throughout the enclosure.

Table 4.5 presents the variation of the horizontal velocity component (U) at three representative locations along the horizontal centreline of the enclosure for different values of the micropolar parameter (K). The remaining governing parameters are kept fixed throughout the computations. The selected monitoring points, namely

TABLE 4.5: Variation of velocity U at different locations for different values of micropolar parameter K.

K	$U(-0.23, 0.0)$	$U(0.0, 0.0)$	$U(0.35, 0.0)$
0.005	0.177403	0.305696	0.0896681
0.05	0.177481	0.305849	0.0897005
0.5	0.177628	0.306849	0.0896356
1.5	0.178302	0.312071	0.0892029
3.5	0.180903	0.329868	0.0880427
5.5	0.187417	0.360866	0.0878845
7.5	0.204667	0.420134	0.0851647

$(-0.23, 0.0)$, $(0.0, 0.0)$, and $(0.35, 0.0)$, correspond to the upstream region, the cavity centre, and the downstream region, respectively. These locations provide a quantitative assessment of the influence of the micropolar coupling parameter on the translational motion of the fluid.

It is observed that increasing the micropolar parameter generally enhances the horizontal velocity in the left and central regions of the cavity. At the left monitoring point, the velocity increases gradually from 0.177403 for $K = 0.005$ to 0.204667 for $K = 7.5$. A more pronounced increase is observed at the cavity centre, where the horizontal velocity rises from 0.305696 to 0.420134 over the same range of K. These results indicate that stronger micropolar coupling promotes the transfer of momentum from the rotating microelements to the surrounding fluid, thereby accelerating the fluid motion in the core region of the enclosure.

In contrast, the velocity at the downstream location, $U(0.35, 0.0)$, exhibits a slight decrease with increasing values of K, reducing from 0.0896681 for $K = 0.005$ to 0.0851647 for $K = 7.5$. This comparatively small reduction suggests that the enhanced rotational motion of the microelements redistributes momentum within the enclosure rather than uniformly increasing the velocity at every location. As a result, momentum is transferred toward the primary circulation region, while a slight reduction occurs near the outlet side of the cavity.

The observed behaviour is consistent with the dimensionless momentum equation governing the horizontal velocity,

$$\frac{\partial U}{\partial T} + U\frac{\partial U}{\partial X} + V\frac{\partial U}{\partial Y} = -\frac{\partial P}{\partial X} + \frac{1}{Re}\left(\frac{\partial^2 U}{\partial X^2} + \frac{\partial^2 U}{\partial Y^2}\right) + \frac{K}{Re}\frac{\partial W}{\partial Y}.$$

It is evident that the micropolar parameter appears explicitly in the coupling term, $\frac{K}{Re}\frac{\partial W}{\partial Y}$, which represents the interaction between the microrotation field and the linear momentum. As K increases, this coupling becomes stronger, allowing angular momentum generated by the rotating microelements to be transferred more effectively to the translational flow. Consequently, the horizontal velocity increases in regions where the microrotation gradients are significant, particularly near the primary circulation and the central portion of the enclosure.

Another noteworthy observation is that the influence of K is spatially non-uniform. The enhancement of the horizontal velocity is much more pronounced at the cavity centre than near the side boundaries. This behaviour indicates that the micropolar effects primarily modify the core circulation, where the interaction between the translational and rotational motions is strongest, whereas the velocity near the downstream boundary remains largely governed by the imposed boundary conditions and the local pressure distribution. Therefore, increasing the micropolar parameter strengthens the overall momentum transport within the enclosure while simultaneously redistributing the flow field through enhanced rotational coupling.

TABLE 4.6: Variation of velocity U at different locations for different values of Eringen number Er.

Er	$U(-0.23, 0.0)$	$U(0.0, 0.0)$	$U(0.35, 0.0)$
0.3	0.177628	0.306849	0.0896356
1.3	0.177522	0.306089	0.0896899
3.3	0.177497	0.305937	0.0896970
5.3	0.177490	0.305899	0.0896986
7.3	0.177487	0.305882	0.0896993

Table 4.6 presents the variation of the horizontal velocity component (U) at three representative locations along the horizontal centreline of the enclosure for different values of the Eringen parameter (Er). The remaining governing parameters are maintained constant throughout the simulations. The selected monitoring points, namely $(-0.23, 0.0)$, $(0.0, 0.0)$, and $(0.35, 0.0)$, correspond to the left, central, and

right portions of the cavity, respectively, enabling a quantitative assessment of the influence of the Eringen parameter on the translational flow.

It can be observed that the Eringen parameter has only a marginal influence on the horizontal velocity distribution. At the left monitoring point, the velocity decreases slightly from 0.177628 for $Er = 0.3$ to 0.177487 for $Er = 7.3$, representing a negligible reduction. A similar trend is observed at the cavity centre, where the horizontal velocity decreases from 0.306849 to 0.305882 as Er increases. In contrast, the velocity at the right monitoring point exhibits a very small increase from 0.0896356 to 0.0896993. The overall variations are extremely small, indicating that changes in the Eringen parameter have only a limited effect on the translational motion of the fluid.

The observed behaviour is consistent with the governing momentum equation,

$$\frac{\partial U}{\partial T} + U\frac{\partial U}{\partial X} + V\frac{\partial U}{\partial Y} = -\frac{\partial P}{\partial X} + \frac{1}{Re}\left(\frac{\partial^2 U}{\partial X^2} + \frac{\partial^2 U}{\partial Y^2}\right) + \frac{K}{Re}\frac{\partial W}{\partial Y}.$$

It is noteworthy that the Eringen parameter does not appear explicitly in the momentum equation. Instead, its influence is indirect through the microrotation field governed by

$$\frac{2K}{Er\,Re}\left(\frac{\partial V}{\partial X} - \frac{\partial U}{\partial Y} - 2W\right).$$

As the Eringen parameter increases, the coupling coefficient $\frac{2K}{ErRe}$ decreases, thereby reducing the interaction between the fluid vorticity and the microrotation field. Consequently, the magnitude of the microrotation velocity decreases, as observed in the previous results. However, because the contribution of the microrotation to the momentum equation is comparatively small under the present flow conditions, the resulting changes in the horizontal velocity remain insignificant.

Another important observation is that the velocity profiles remain nearly unchanged at all monitoring locations despite the noticeable reduction in the microrotation field with increasing Er. This indicates that the global flow circulation is primarily

governed by the imposed boundary conditions, Reynolds number, and viscous effects, whereas the Eringen parameter mainly regulates the rotational behaviour of the microstructural elements without substantially altering the translational flow. Therefore, increasing the Eringen parameter weakens the rotational response of the microelements but has only a secondary influence on the horizontal velocity distribution within the enclosure.

Chapter 5

Conclusion and Future Directions

The main findings of this investigation are concluded in the following section.

5.1 Conclusion

This thesis presented a numerical investigation of transient mixed convection micropolar fluid flow and heat transfer in a two-dimensional enclosure using the Galerkin Finite Element Method (FEM). The governing equations consisting of the continuity equation, momentum equations, microrotation equation, and energy equation were first transformed into their corresponding weak (variational) forms using the Galerkin weighted residual approach. The resulting weak formulation was discretized using finite element basis functions, while the temporal derivatives were approximated using the implicit backward Euler scheme. The numerical algorithm was successfully implemented in `FreeFEM++` to obtain stable and accurate solutions for the coupled nonlinear system.

The accuracy of the developed finite element formulation was verified by simulating the classical lid-driven cavity problem in the absence of thermal transport, mixed convection, and microrotation effects. The computed velocity profiles showed excellent agreement with the benchmark results reported by Ghia *et al.*, thereby validating both the mathematical formulation and its implementation in `FreeFEM++`. This validation established confidence in the numerical methodology before extend-

ing it to the complete mixed convection micropolar flow model.

A comprehensive parametric study was carried out to investigate the influence of the Reynolds number (Re), Prandtl number (Pr), micropolar coupling parameter (K), and Eringen parameter (Er) on the flow and thermal characteristics. The numerical results demonstrated that the Reynolds number strongly influences the momentum transport within the enclosure. Increasing Re enhanced the dominance of inertial forces over viscous forces, resulting in stronger flow circulation, larger velocity gradients, and thinner momentum boundary layers.

The thermal behaviour of the fluid was found to be significantly affected by the Prandtl number. Increasing Pr reduced the thermal diffusivity, causing the temperature field to become increasingly confined near the heated wall. Consequently, thinner thermal boundary layers and steeper temperature gradients were observed, indicating enhanced local heat transfer.

The micropolar coupling parameter K was shown to play a dominant role in governing the rotational behaviour of the fluid. Larger values of K considerably increased the magnitude of the microrotation field by strengthening the coupling between the translational and angular momentum equations. This enhanced rotational motion also influenced the velocity distribution by promoting momentum exchange between the microstructural elements and the surrounding fluid, leading to stronger circulation within the enclosure.

In contrast, increasing the Eringen parameter weakened the interaction between the fluid vorticity and the microrotation field. Consequently, the magnitude of the microrotation velocity decreased throughout the enclosure, while only minor changes were observed in the translational velocity field. These results indicate that the Eringen parameter primarily controls the rotational response of the microelements without substantially altering the overall flow structure.

The contour plots and quantitative comparisons at selected monitoring locations consistently demonstrated the influence of the governing dimensionless parameters on the flow and thermal characteristics. The numerical results further confirmed

that the interactions among inertial forces, buoyancy effects, thermal diffusion, and micropolar rotational dynamics significantly affect the transport of momentum and heat within the enclosure.

Overall, the present study demonstrates that the Galerkin finite element method implemented in `FreeFEM++` provides an accurate, robust, and computationally efficient framework for the numerical simulation of transient mixed convection micropolar flows. The developed numerical model can be extended to investigate more complex transport phenomena involving non-Newtonian fluids, porous media, magnetic fields, nanofluids, or chemically reactive flows. Therefore, the present work provides a reliable computational foundation for future studies on advanced heat transfer and fluid flow problems encountered in engineering and industrial applications.

5.2 Future Work

The present work may be extended in several directions to investigate more complex physical phenomena. Some possible future research directions are as follows:

i. Extend the numerical model to three-dimensional mixed convection micropolar flows.

ii. Incorporate magnetic field effects (MHD) to study electrically conducting micropolar fluids.

iii. Investigate micropolar nanofluids by including nanoparticle transport mechanisms such as Brownian motion and thermophoresis.

iv. Introduce thermal radiation, Joule heating, viscous dissipation, and internal heat generation effects into the governing equations.

v. Study mixed convection in porous media using Darcy–Brinkman or Darcy–Forchheimer models.

vi. Employ adaptive mesh refinement and higher-order finite elements to improve computational accuracy and efficiency.

vii. Compare the Galerkin finite element solutions with other numerical techniques

such as finite volume, spectral element, or lattice Boltzmann methods.

viii. Investigate transient heat transfer under different cavity geometries, moving boundary conditions, and non-uniform heating configurations.

Bibliography

[1] F. P. Incropera, D. P. DeWitt, T. L. Bergman, and A. S. Lavine, "Fundamental of heat and mass transfer", 8th ed. John Wiley Sons, 2017.

[2] A. Bejain, "Convection Heat Transfer", 4th ed. John Wiley Sons, 2013.

[3] W. M. H. K. Versteeg, "An introduction to Computational Fluid Dynamics: The Finite Volume Method", 2nd ed. Pearson Education Limited, 2007.

[4] A. Al-Amiri *et al.*, "Heat transfer in cavities: Configurative systematic review," *Energies*, vol. 16, no. 5, p. 2338, 2023.

[5] S. Ostrach, "Natural convection in enclosures," *International Journal of Heat Transfer*, vol. 110, pp. 1175–1190, 1988.

[6] . P. B. H. Chandra, "Buoyancy-induced convective flow and heat transfer over obstacles embedded inside a cu–water nanofluid-saturated porous cavity," *Numerical Heat Transfer, Part A: Applications*, vol. 83, pp. 726–744, 2023.

[7] A. C. Eringen, "Theory of micropolar fluids," *Journal of Mathematics and Mechanics*, vol. 16, no. 1, pp. 1–18, 1966.

[8] G. Lukaszewicz, "Micropolar Fluids: Theory and Applications". Birkhaauser, Boston,Massachusetts,USA, 1999.

[9] O. C. Zienkiewicz, R. L. Taylor, and J. Z. Zhu, "The Finite Element Method: Its Basis and Fundamentals", 7th ed. Elsevier, 2013.

[10] J. N. Reddy, "An introduction to the Finite Element Method", 3rd ed. McGraw-Hill, 2006.

[11] . A. H. J. Donea, "Finite Element Methods for flow problems". John Wiley Sons, 2003.

[12] B. Szabo and I. Babuska, "Finite Element Analysis: Method, Verification and Validation". John Wiley Sons, 2021.

[13] F. Hecht, "New development in freefem++," *Journal of Numerical Mathematics*, vol. 20, no. 3–4, pp. 251–265, 2012. [Online]. Available: https://freefem.org/

[14] A. H. M. S. I. A. A. . N. F. Y. Khan, R. Mahmood, "Finite element simulations of inclined magnetic field and mixed convection in an enclosure with periodically heated walls in the presence of an obstacle," *Frontiers in Physics*, vol. 10, 2022.

[15] . K. J. C. S. Reddy, V. R. Prasad., "Numerical simulation of natural convection heat transfer from a heated square cylinder in a square cavity filled with micropolar fluid," *International Journal of Heat transfer*, vol. 50, pp. 5267–5285, 2021.

[16] I. K. . K. S. N. M. A. Siddiqui, A. Riaz, "Augmentation of mixed convection heat transfer in a lid assisted square enclosure utilizing micropolar fluid under magnetic environment: A numerical approach," *Results in Physics*, vol. 18, 2020.

[17] P. B. . H. S. T. L. Kumar, R. Bhargava, "Finite element solution of mixed convection micropolar fluid flow between two vertical plates with varying temperature," *Archives of Mechanics*, vol. 57, pp. 251–274.

[18] S. K. Jena and S. P. Bhattacharyya, "The effect of microstructure on the thermal convection in a rectangular box of fluid heated from below," *International Journal of Engineering Science*, vol. 53, pp. 69–76, 1986.

[19] T. H. Hsu and C. K. Chen, "Natural convection of micropolar fluids in a rectangular enclosure," *International Journal Of Engineering Science*, vol. 34, no. 4, pp. 407–417, 1996.

[20] S. G. Wang and T. H. Hsu, "Natural convection of micropolar fluids in an inclined rectangular enclosure," *Mathematical and Computer Modelling*, vol. 17, no. 10, pp. 73–80, 1993.

[21] M. A. A. M. M. Rahman and M. A. H. Mamun, "Finite element analysis of mixed convection in a rectangular cavity with a heat-conducting horizantal circular cylinder," *Non linear Analysis: Modelling and Control*, vol. 14, no. 2, pp. 217–247, 2009.

[22] S. H. H. A. J Chamkha. and Q. R. Abd-Amer, "Mixed convection heat transfer of air inside a square vented cavity with a heated horizantal square cylinder," *Numerical Heat Transfer, Part A: Applications*, vol. 59, pp. 58–79, 2011.

[23] H. F. Öztop and Dağtekin, "Mixed convection in two-sided lid-driven differentially heated square cavity," *International Journal of Heat and Mass Transfer*, vol. 47, no. 8-9, pp. 1761–1769, 2004.

[24] M. A. S. N. S. Gibanov and I. Pop, "Free convection in a trapezoidal cavity filled with a micropolar fluid," *International Journal of Heat and Mass Transfer*, vol. 99, pp. 831–838, 2016.

[25] A. M. Rashad, "Influence of magnetic field and internal heat generation on mixed convection of a micropolar fluid in a lid-driven cavity," *Journal of the Egyption Mathematical Society*, vol. 24, pp. 840–850, 2016.

[26] F. Selimefendigil and H. F. Öztop, "Mixed convection in a lid-driven cavity with different shaped obstacles," *International Journal of Mechanical Sciences*, vol. 140, pp. 396–408, 2018.

[27] R. Mohebbi, "Natural convection fluid flow and heat transfer in a square cavity with a heated triangular obstacle using finite element method," *Journal of Modeling in Engineering*, vol. 16, pp. 361–373, 2018.

[28] P. K. S. . I. P. T. Basak, S. Roy, "Analysis of mixed convection flows within a square cavity with uniform and non-uniform heating of bottom wall," *International Journal of Thermal Sciences*, vol. 48, pp. 891–912, 2009.

[29] K. V. K. Khanafer and M. Lightstone, "Buoyancy-driven heat transfer enhancement in a two-dimensional enclosure utilizing nanofluids," *International Journal of Heat and Mass Transfer*, vol. 46, no. 19, p. 3639–3653, 2003.

[30] O. Aydin and L. Pop, "Natural convection in a differentially heated enclosure filled with a micropolar fluid," *International Journal of Thermal Sciences*, vol. 46, no. 10, pp. 963–969, 2007.

[31] M. I. K. A. A. T. H. M. Waqas, M. Farooq and T. Yasmeen, "Magnetohydrodynamic (mhd) mixed convection flow of micropolar liquid due to nonlinear stretched sheet with convective condition," *International Journal of Heat and Mass Transfer*, vol. 102, pp. 766–772, 2016.

[32] M. Sulaiman, N. A. Khan, F. S. Alshammari, and G. Laouini, "Performance of heat transfer in micropolar fluid with isothermal and isoflux boundary conditions using supervised neural networks," *Mathematics*, vol. 11, no. 5, p. 1173, 2023.

[33] J. N. Reddy and D. K. Gartling, "The Finite Element Method in Heat Transfer and Fluid Dynamics,", 3rd ed. Boca Raton, FL, USA: CRC Press, 2010.

[34] D. K. Sahoo and B. V. Rathish Kumar, "A variational multiscale stabilized finite element method for double diffusive incompressible flow with application to mixed convection in a heated staggered cavity under magnetic field," *International Journal for Computational Methods in Engineering Science and Mechanics*, vol. 26, no. 2, pp. 140–154, 2024.

[35] U. Ghia, K. N. Ghia, and C. T. Shin, "High-re solutions for incompressible flow using the navier-stokes equations and a multigrid method," *Journal of Computational Physics*, vol. 48, no. 3, pp. 387–411, 1982.

[36] Y. W. Kwon and H. Bang, "The finite Element Method using MATLAB", 2nd ed. CRC Press, Boca Raton London New York Washington, D. C., 2000.